ANALYTICAL AND COMPUTATIONAL STUDY OF ELECTRON BUNCH DYNAMICS

By

Xukun Xiang

A DISSERTATION

Submitted to
Michigan State University
in partial fulfillment of the requirements
for the degree of

Physics – Doctor of Philosophy

2020

ABSTRACT

ANALYTICAL AND COMPUTATIONAL STUDY OF ELECTRON BUNCH DYNAMICS

By

Xukun Xiang

This dissertation is centered on the analytical and numerical study of ellipsoidal electron bunch dynamics. We are particularly interested in the focusing process of the probing electron bunches in the ultrafast electron diffraction/microscopy system, so that we can improve the temporal and spectral resolution of the ultrafast experiments.

More specifically, to understand the collective space charge effects throughout the bunch evolution, we employed several analytic models to describe the bunch dynamics. We start with an extension of the mean-field model using ordinary differential equations. Analysis of this mean-field model leads to the identification of a longitudinal critical chirp, which separates two regimes for particle trajectories for the longitudinal focusing of the bunches: bounce-back, where the particles reverse their direction at the waist of the focusing process, and cross-over, where the bunch experiences a singularity where the bunch width reduces to zero. We show that time can be scaled by the initial plasma frequency, and the critical chirp becoming dimensionless and solely depend on the initial bunch aspect ratio.

In order to study the emittance effect on the bunch dynamics, we introduce the self-similar analytical (SSA) model, a statistical method describing the second order moments dynamics to model the evolution of an ellipsoidal electron bunch. We also discussed its linear chirp assumption, explaining how it is the key assumption that leads to the emittance conservation according to the SSA model. We discuss the statistical nature of bunch emittance noting that the space charge effect of the uniform density profile and of the Gaussian

profile are close to each other in the SSA model. The impact from a changing emittance is captured by an additional term in the modified SSA model, which is then equivalent to the Kapchinsky-Vladimirsky (K-V) envelope equation in accelerator physics. We point out that the application of the statistical methods can extend beyond the uniform ellipsoidal bunch, while the accuracy of the SSA prediction is mainly related to the discrepancy between the actual density profile and the uniform density profile.

We present the Molecular Dynamics (MD) simulation results for the longitudinal focusing process of uniform spheroidal electron bunches. The comparison of the longitudinal width evolution between the MD simulations and the SSA predictions shows the impact of a varying emittance on bunch evolution. We propose two competing mechanisms for the change of emittance throughout the compression process. The disorder-induced heating (DIH) increases the emittance in both degrees of freedom while the difference in the SSA temperature generates emittance transfer between degrees of freedom. In addition, the non-uniform density profile at the focal point introduces significant DIH that increases the emittance in both the longitudinal and transverse directions, which can be a contributing factor for the Boersch effect observed in bunched beams.

Here is the dedication

ACKNOWLEDGMENTS

Here is the acknowledgement

TABLE OF CONTENTS

LIST OF FIGURES

KEY TO ABBREVIATIONS

Here are some abbreviations and acronyms that appear in this dissertation. The full name is shown in the first appearance of each abbreviation. For a better reading experience and ease of reference, the list of abbreviations used in this work are summarized below in alphabetical order.

AG . . . . Analytic Gaussian

DIH . . . . Disorder-induced heating

EOM . . . . . . Equation(s) of motion

FMM . . . . . . Fast multipole method

MD . . . . Molecular dynamics

MFT . . . . . . Mean-field theory

KDE . . . . . . Kernel density estimation

K-V . . . . Kapchinsky-Vladimirsky

RF . . . . Radio-frequency

rms . . . . Root mean square

SSA . . . . Self-similar analytical

UED . . . . . . Ultrafast electron diffraction

UEM . . . . . . Ultrafast electron microscopy

Chapter 1

Introduction

The time scale of fascinating phenomena in the physics world ranges from millions of years in cosmology to infinitesimally fractions of seconds in ultrafast phase-transitions and nuclear reactions. [1,2] To truly understand the fundamental physics behind these intriguing phenomena, we need the ability to record the evolution of these systems of interest at high enough resolution in both the time and space domains. Particularly, resolving the atomic motions throughout phase-transitions leads to the understanding of critical phase-transition mechanisms in condensed matter physics [3–5]. To fully describe the phase-transitions with a sub-picosecond time-scale, we need to have the ability to resolve the temporal resolution at tens of femtoseconds.

1.1 The Ultrafast Electron Microscopy

In practice, many of ultrafast phase-transitions are explored experimentally using ultrafast microscopies with the so-called "pump-probe" scheme [6–11]. As the name suggests, these experiments consist of two kinds of pulses interacting with the system of interest, the pump pulse and the probe pulse. A pump pulse comes first as the perturbation to the system of interest. With the excitation from the pump pulse, the system goes through the phase-transition that we would like to explore. A probe pulse then interacts with the system at a later time to produce a snapshot of the system at that specific delay time. This pump and

probe process is then repeated numerous times with various delay times to obtain the time evolution of the system throughout the phase-transition. In order to resolve these ultrafast phenomena, both the pump and probe pulses need to be sufficiently short in time comparing to the time-scale of the phase-transition process. In addition, for regular ultrafast microscopies, the energy deposition of the pump and probe pulses are limited so that the system is capable of going through the same phase-transition and recovering numerous times at a reasonable repetition rate.

We are working with the ultrafast research group at Michigan State University, using a femtosecond laser as the pump pulse to excite the system and the electron bunches as the probe pulse to measure the system response throughout the phase-transition [12–17]. For ultrafast electron microscopy (UEM), enough electrons are needed to generate a pattern with good signal-noise ratio, which translates to roughly 10^5 to 10^7 electrons in one single probe pulse for diffraction and 10^7 to 10^9 electrons for imaging. [1]

Compressing a bunch with such a high number of electrons introduces technological hurdles as the space charge effects[1] on the probing electron bunch are significant at specific locations within the microscopy column due to the bunch's huge electron density at those locations [13–19]. Magnetic lenses are used to mitigate the space-charge effect induced expansion in transverse direction, while the longitudinal focusing of the electron bunch is achieved using radio frequency (RF) cavities. The schematic design of the beamline is illustrated in Fig. 1.1(a) and further details can be found in the publications from the Ruan Group [3, 15, 18, 20].

---

[1]Here the space charge effect is referring to the strong Coulomb interaction between electrons within the bunch.
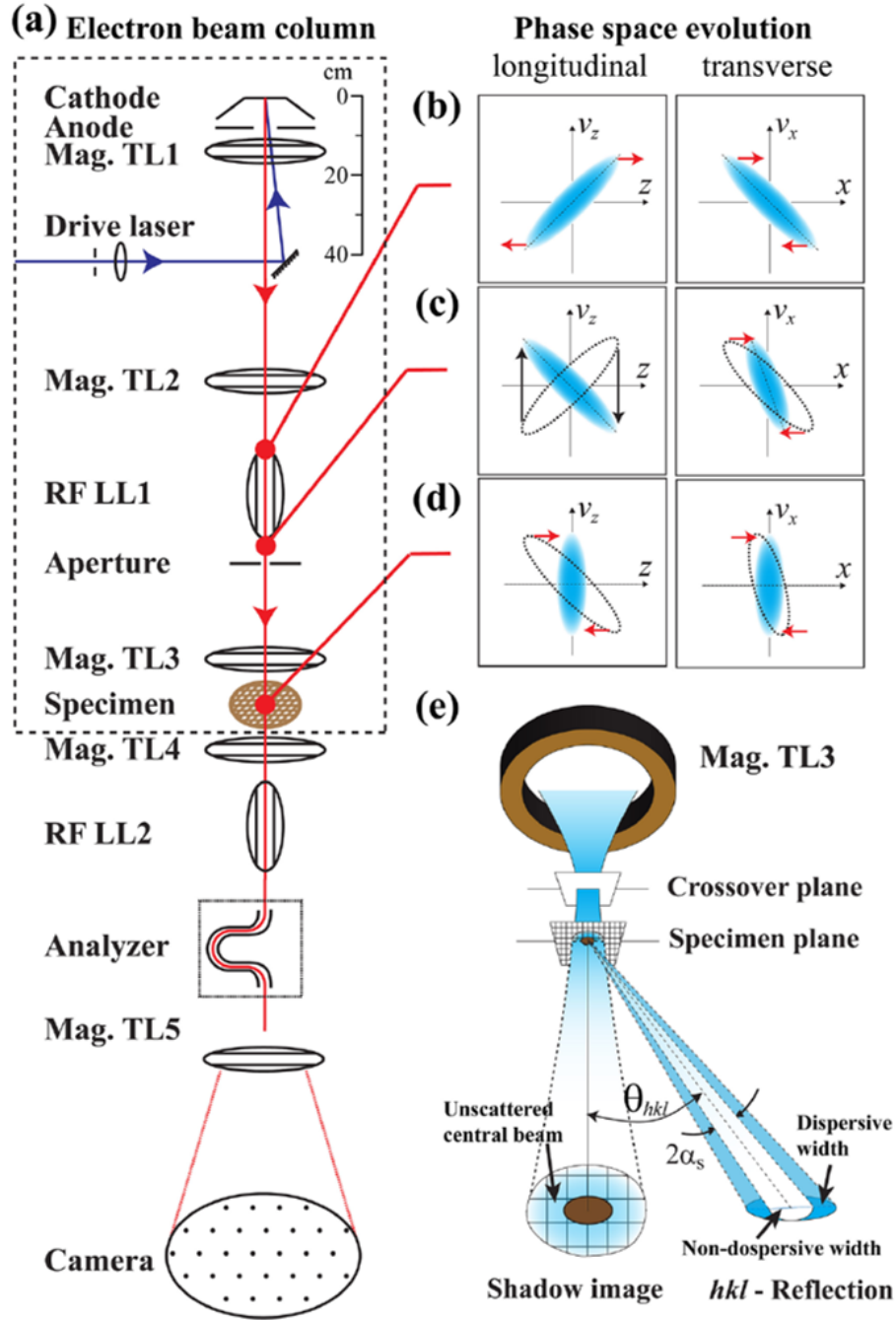
Figure 1.1: Ultrafast electron beam column with optics for controlling electron bunch phase space evolution. (a) Schematic drawing of a prototype UEM beamline. (b)–(d) The phase space evolution in the injector portion of the beamline (enclosed in dashed line). (e) The conceptual outline of the atomic grating approach to characterize the energy spread of the electron bunches. Adapted from "Active control of bright electron beams with RF optics for femtosecond microscopy" by Williams, J. et. al., 2017, *Structural Dynamics, 4(4)*, 044035.

1.2 Importance of our analytical modeling

As the title of this dissertation suggests, we are interested in the analytical modeling for the evolution of the probing electron bunch, which is critical to the design of next generation technologies. Simple analytic models are particularly helpful for improving instrument design.

We focus our analytical study on the uniform ellipsoidal electron bunch, which is an ideal theoretical object in systems governed by gravitational or Coulomb interactions [21]. The importance of the uniform ellipsoidal bunch comes from its well-behaved linear self-field, which leads to the maintenance of the uniform charge density profile as the bunch evolves [22]. In accelerator physics, such a uniform distribution is a prerequisite in employing techniques such as emittance compensation [23] as well as providing the basis of other theoretical analyses [17]. It has long been proposed that such a uniform ellipsoid may be generated through proper control of the transverse profile of a short charged-particle bunch emitted from a source into vacuum [21, 24–26], and experimental results have shown that an electron cloud emitted from a photocathode and rapidly accelerated into the highly-relativistic regime can develop into a final ellipsoidal profile characteristic of a uniform charge distribution [27].

Although we have numerical simulations to illustrate the detailed phase-space distribution of the electron bunch throughout the evolution, analytical study such as the methods in this dissertation provides valuable insights about the underlying physics behind the interesting behavior of the bunches. In addition, the new concepts from the analytical modeling are helpful to better understanding emittance evolution and the Boersch effect, which is crucial to improve the performance of ultrafast experiments.

1.3   The Existing analytical models

Currently, the second-order statistics and the corresponding derivative statistics (namely, the rms emittance) are the key measurements for improving the performance of the probing electron bunch. The spatial variance in the longitudinal direction is related to the pulse duration of the electron probe, which is essential to the temporal resolution of the probe measurement. The variance of longitudinal momentum is another key second-order statistics, determining the spectral resolution of the probing electron bunch. Therefore, the existing analytical methods are oriented to present their predictions for the bunch evolution using the trajectories of those second order statistics.

The difference in calculation perspective divides the existing models into two categories: the mean-field theory (MFT) and the statistical methods. The MFT assumes a uniform density profile and calculates the time derivatives of the bunch statistics based on that assumption, i.e. the uniform density profile is the cornerstone of the bunch evolution in the MFT. On the contrary, the statistical methods propagate the electron bunch evolution from the time-derivatives of those second-order bunch statistics. The force related terms in the time-derivatives of the bunch statistics are calculated based on the assumption/estimation of the transient density profile, which is not restricted to one specific type of function. For example, the density profile can be a uniform bunch for Kapchinsky-Vladimirsky (K-V) envelope equations or a Gaussian bunch for the Analytic Gaussian (AG) model. Furthermore, the density profile is not required to retain the same type during the evolution as the expression of the force is one of the components to calculate the time derivatives. The driving factor in the statistical methods is the time derivatives of the bunch statistics, not the specific density profile. Here is the brief overview of the three existing models that we

will discuss in detail later.

The mean-field theory has been utilized in the astrophysics and Coulomb explosion literature where the mean-field effects of a uniform ellipsoidal electron bunch yield ordinary differential equations for the bunch statistics. Specifically, Lin et al. developed a model for gravitational collapse of a spheroidal ellipsoid that could be written as a system of differential equations for the longitudinal and transverse width of the bunch [28]. Similar techniques regarding the repulsive electrostatic force between the electrons were developed to model Coulomb explosion from rest [22, 29], which is similar to a time reversed version of the gravitational collapse. Both techniques require a uniform ellipsoid throughout their evolution.

Michalik and Sipe introduced the Analytic Gaussian (AG) model that predicts not only the spatial width evolution but also the full phase space evolution [30–32], with the assumption that the bunch retains its Gaussian density profile throughout the evolution. As we will discuss in detail later in Sec.3.3.2, the AG model can be considered as an intermediate approach between the MFT and the statistical methods. Since AG's Gaussian density profile uses the three second-order statistics as parameters, the formulation of the AG model appears to focus on the dynamics of the three bunch statistics while the original derivation of the AG model is more similar to that of the MFT.

As an example of the statistical methods, the well-established Kapchinsky-Vladimirsky (K-V) envelope equations were initially developed to describe the evolution of uniform continuous beams [33] in the accelerator physics community. Sacherer provided a simple perspective which showed that the K-V envelope equations could be derived from basic statistical considerations with applications of the mean-field force from a uniform distribution [34]. The mathematical form of both the MFT and the AG model can also be derived from the

6

K-V envelope equations with similar considerations of unifrom or Gaussian density profile, respectively [35].

1.4   Overview

The central focus of this dissertation is to gain more insight into the evolution of the probing electron bunch from studying the analytical models and numerical simulations. Here is the detailed structure of this dissertation.

In Chapter 2, we overview the mean-field theory (MFT) for studying the compression process of uniform ellipsoidal electron bunches. MFT provides the expression for electrostatic potential inside uniform and Gaussian ellipsoidal bunches, as well as the evolution prediction for zero-emittance uniform bunches. C.C. Lin [28] and Grech et. al., [22] first proposed the MFT formalism for uniform bunch evolution from rest. We extend this model by adding a linear chirp. As a result of this modification, we propose a method that enables researchers to study the crossover phenomena of bunch focusing and its effects on the evolution of ellipsoidal electron bunches.

In Chapter 3, we use statistical methods to model the evolution of an electron bunch, particularly a self-similar analytical model. Statistical methods predict the evolution of ellipsoidal bunches through the time derivatives of bunch statistics, which overcomes the limitation of MFT and the AG model assumptions of the bunch density distribution profile. We propose the self-similar analytical model, which builds on the MFT and the Analytic Gaussian model. This new model and its expanded model contributes to the field, as it includes the effect of varying emittance on the evolution of electron bunches. We also discussed the relationship between the SSA model and the K-V envelope equations.

In Chapter 4, we compare the predictions of the SSA model to numerical simulations for ellipsoidal bunch compression. In particular, we discuss the impact of varying emittance on bunch evolution and our understanding of Boersch effect. Moreover, we developed a simulation code, using it in the electron bunch compression process.

Chapter 5 presents the conclusions and disucssion. In particular, we discuss the directions for future research, such as developing analytic models for emittance growth and the Boersch effect, given the importance of these two concepts on bunch evolution.

Chapter 2

Mean-field theory for dynamics of ellipsoidal electron bunches

In this chapter, we propose a mean-field theory (MFT) to describe evolution of an ellipsoidal probing electron bunch in ultrafast experiments. We first review the mean-field theory for uniform ellipsoidal bunches and then we discuss the evolution of a Gaussian bunch. We conclude this chapter by discussing the underlying assumptions of the MFT such as the linearity assumption and self-similar evolution.

2.1   Mean-field Theory for a uniform spheroidal bunch

For modeling electron bunch evolution, the majority of existing UEM literature discusses uniform distributions, which stems from general potential theories regarding both gravitational [28] and Coulomb interactions [21, 22]. The advantage of working with uniform bunch dynamics is that they evolve self-similarly. In other words, the uniform bunch stays uniform throughout the evolution. This self-similar evolution greatly simplifies the modeling process and the bunch evolution can be captured by tracking the bunch size parameter in each direction. The self-similar evolution comes from the linear self field inside the uniform bunch. As Lin et. al, pointed out in their paper for gravitational collapse [28], the essence is that the potential within a uniform spheroid is quadratic in Cartesian coordinates, i.e., the self

field linearly depends on the spatial position. For Coulomb interactions, in electron bunches, a similar idea was applied to study Coulomb explosion from rest with zero emittance and achieved good agreement with numerical simulations [22, 29].

To provide necessary context for understanding the MFT, we first review the non-relativistic MFT for a uniform spheroidal bunch, and demonstrate how linear initial chirps, i.e. the linear correlation between momentum and position, can be added into the model to describe the bunch focusing process. Here, the bunch focusing is referring to the temporal compression of the probing electron bunch by an radio-frequency(RF) cavity, or a transverse compression by a magnetic focusing lens along the beamline. Also, details about the initial conditions are examined, and the discussion naturally leads to the identification of a critical chirp that demarcates two qualitatively different regimes of bunch behavior according to MFT: "bounce-back" where electrons reverse their motion and never cross the bunch center and "cross-over" where electrons cross the bunch center.

2.1.1   Mean-field theory for a uniform ellispoidal bunch

The mean-field theory we are referring to here, treats the electron bunch as an ideal homogeneous continuum object. This simplification can be considered as taking the continuum limit of the actual bunch consisting of a finite number of discrete electrons in the experiments and simulations, i.e. MFT is essentially modeling a bunch with N identical particles where $N \to \infty$ and each particle carries charge amount Q/N, with Q being the total charge of the entire bunch. Thanks to this simplification, all the nice features of mean-field theory are applicable to the uniform electron bunch, while the limitation of this simplification will be discussed later. The following derivation of the Coulomb potential and field for uniform ellipsoids are generally based on Chapter 2 in MacMillan's book [36] for the gravitational

interaction.

The surface of a given ellipsoid with semi-axes (a, b, c) is defined by equation:

$$\frac{\xi^2}{a^2} + \frac{\eta^2}{b^2} + \frac{\zeta^2}{c^2} = 1 \qquad (2.1)$$

Let the interior point for which the potential is to be computed be $P(x, y, z)$. On taking P as the origin of a spherical coordinates system (ρ, φ, θ) with the transformation:

$$\xi = x + \rho \cos \varphi \cos \theta \qquad (2.2a)$$

$$\eta = y + \rho \cos \varphi \sin \theta \qquad (2.2b)$$

$$\zeta = z + \rho \sin \varphi \qquad (2.2c)$$

and the corresponding charge element

$$dq = \rho_c \rho^2 \cos \varphi d\varphi d\theta d\rho \qquad (2.3)$$

with the volume charge density $\rho_c = n \cdot e$ (typically n is the electron number density). Then, the electrostatic potential at point P (with respect to the potential zero point at infinity) is expressed as:

$$V(x, y, z) = \frac{\rho_c}{4\pi\varepsilon_0} \int_E \frac{dq}{\rho} = \kappa \int_{-\frac{\pi}{2}}^{+\frac{\pi}{2}} \int_0^{2\pi} \int_0^{\rho_1(\theta,\varphi)} \rho \cos \varphi d\varphi d\theta d\rho \qquad (2.4)$$

We substitute $\kappa = \frac{\rho_c}{4\pi\varepsilon_0}$ to simplify the derivation.

The upper limit $\rho_1(\theta, \varphi)$ of the integration with respect to ρ is a function of θ and φ, since the integration is from P to a point on the surface of the ellipsoid. So, we can insert

11

Eq. 2.2a into Eq.2.1 for ρ_1 as:

$$A\rho_1^2 + 2B\rho_1 + C = 0 \tag{2.5}$$

where

$$A = \frac{\cos^2\varphi\cos^2\theta}{a^2} + \frac{\cos^2\varphi\sin^2\theta}{b^2} + \frac{\sin^2\varphi}{c^2} \tag{2.6a}$$

$$B = \frac{x\cos\varphi\cos\theta}{a^2} + \frac{y\cos\varphi\sin\theta}{b^2} + \frac{z\sin\varphi}{c^2} \tag{2.6b}$$

$$C = \frac{x^2}{a^2} + \frac{y^2}{b^2} + \frac{z^2}{c^2} - 1 \tag{2.6c}$$

After a lengthy derivation,[1] we can have

$$
\begin{aligned}
V = \kappa \int_{-\frac{\pi}{2}}^{+\frac{\pi}{2}} \int_0^{2\pi} \left(\frac{\cos^2\varphi\cos^2\theta}{a^2} \cdot \frac{x^2}{a^2} + \frac{\cos^2\varphi\sin^2\theta}{b^2} \cdot \frac{y^2}{b^2} + \frac{\sin^2\varphi}{c^2} \cdot \frac{z^2}{c^2} \right) \frac{\cos\varphi\,d\varphi\,d\theta}{A^2} \\
- \frac{\kappa}{2} C \int_{-\frac{\pi}{2}}^{+\frac{\pi}{2}} \int_0^{2\pi} \frac{\cos\varphi\,d\varphi\,d\theta}{A}
\end{aligned}
\tag{2.7}
$$

To simplify the above expression, one may use the following:

$$W = \frac{\kappa}{2} \int_{-\frac{\pi}{2}}^{+\frac{\pi}{2}} \int_0^{2\pi} \frac{\cos\varphi\,d\varphi\,d\theta}{A} \tag{2.8}$$

The simplified form of the potential then reduces to:

$$
\begin{aligned}
V &= \frac{1}{a}\frac{\partial W}{\partial a}x^2 + \frac{1}{b}\frac{\partial W}{\partial b}y^2 + \frac{1}{c}\frac{\partial W}{\partial c}z^2 - CW \\
&= \left(\frac{1}{a}\frac{\partial W}{\partial a} - \frac{W}{a^2} \right)x^2 + \left(\frac{1}{b}\frac{\partial W}{\partial b} - \frac{W}{b^2} \right)y^2 + \left(\frac{1}{c}\frac{\partial W}{\partial c} - \frac{W}{c^2} \right)z^2 + W
\end{aligned}
\tag{2.9}
$$

Since W is a function of the semi-axes (a, b, c), then so are all of its derivatives. Therefore, the coefficients of the quadratic term x^2, y^2 and z^2 are functions of a, b, and c only. Also,

---

[1]The detailed derivation can be found in the Appendix

W is the potential at the center of the ellipsoid if taking $P(x, y, z) = (0, 0, 0)$. W can be further reduced to the following form,[2]

$$W = \pi \kappa a b c \int_0^\infty \frac{ds}{\sqrt{(a^2 + s)(b^2 + s)(c^2 + s)}}. \tag{2.10}$$

Thus the term related to the derivative of W with respect to a reads:

$$\frac{1}{a} \frac{\partial W}{\partial a} - \frac{W}{a^2} = \frac{\pi \kappa a b c}{a^2} \int_0^\infty \left(\frac{\partial a (a^2 + s)^{-\frac{1}{2}}}{\partial a} - \frac{1}{\sqrt{a^2 + s}} \right) \frac{ds}{\sqrt{(b^2 + s)(c^2 + s)}}$$
$$= -\pi \kappa a b c \int_0^\infty \frac{1}{a^2 + s} \frac{ds}{\sqrt{(a^2 + s)(b^2 + s)(c^2 + s)}} \tag{2.11}$$

Therefore, the potential inside of a uniform ellipsoidal electron bunch may be expressed as:

$$V(x, y, z) = \frac{\rho_c}{4\varepsilon_0} a b c \int_0^\infty \left(1 - \frac{x^2}{a^2 + s} - \frac{y^2}{b^2 + s} - \frac{z^2}{c^2 + s} \right) \frac{ds}{\sqrt{(a^2 + s)(b^2 + s)(c^2 + s)}} \tag{2.12}$$

with the zero point of potential at infinity.

The corresponding electrostatic field at the interior point $P(x, y, z)$ is,

$$\vec{E}(x, y, z) = E_x \hat{x} + E_y \hat{y} + E_z \hat{z} \tag{2.13}$$

with $\hat{x}$, $\hat{y}$, and $\hat{z}$ representing the unit vectors, respectively. The components of the field can

---

[2]The detailed derivation can be found in the Appendix

be represented by the following equations:

$$E_x(x, y, z) = x \cdot \frac{\rho_c abc}{2\varepsilon_0} \int_0^\infty \frac{ds}{(a^2 + s)\sqrt{(a^2 + s)(b^2 + s)(c^2 + s)}} \tag{2.14a}$$

$$E_y(x, y, z) = y \cdot \frac{\rho_c abc}{2\varepsilon_0} \int_0^\infty \frac{ds}{(b^2 + s)\sqrt{(a^2 + s)(b^2 + s)(c^2 + s)}} \tag{2.14b}$$

$$E_z(x, y, z) = z \cdot \frac{\rho_c abc}{2\varepsilon_0} \int_0^\infty \frac{ds}{(c^2 + s)\sqrt{(a^2 + s)(b^2 + s)(c^2 + s)}} \tag{2.14c}$$

Specifically for spheroids, we introduce the radial coordinate, r, to take advantage of the rotational symmetry of spheroids. The radial coordinate r is expressed as:

$$r = \sqrt{x^2 + y^2} \tag{2.15}$$

Although the detailed calculations below are for prolate spheroids ($a = b < c$), similar results are valid for general, uniformly charged ellipsoidal bunches. We can then rewrite the electrostatic field (Eq.2.14) as a linear function of the cylindrical coordinates, as follows:

$$\vec{E}(r, z) = E_r(r)\hat{r} + E_z(z)\hat{z} \tag{2.16}$$

with $\hat{r}$ and $\hat{z}$ representing the radial and longitudinal unit vectors, respectively, and

$$E_r(r) = \frac{\rho_c}{2\varepsilon_0}\xi_r(\alpha) \cdot r \tag{2.17a}$$

$$E_z(z) = \frac{\rho_c}{2\varepsilon_0}\xi_z(\alpha) \cdot z \tag{2.17b}$$

where the spheroid aspect ratio α is defined as:

$$\alpha = \frac{a}{c} \tag{2.18}$$

and where the corresponding geometry coefficients are

$$\xi_r(\alpha) = \alpha^2 \int_0^\infty \frac{ds}{(\alpha^2 + s)^2 (1 + s)^{1/2}} \tag{2.19a}$$

$$\xi_z(\alpha) = \alpha^2 \int_0^\infty \frac{ds}{(\alpha^2 + s)(1 + s)^{3/2}} \tag{2.19b}$$

Based on Eq.2.17 to 2.19, we can get the equations of motion through the aspect ratio of the bunch, and the entire bunch evolution history can be obtained with proper initial conditions.

2.1.2 Self-Similar Evolution and Equations of Motion

Before we discuss the equations of motion for the bunch evolution, we need to discuss the self-similar assumption that enables this simple MFT formalism. The linear dependence of the electrostatic field on spatial position results in the preservation of bunch uniformity provided that the initial momentum-position profile does not start out non-linear. In other words, the charge density must be homogeneous across the bunch, while the bunch size and aspect ratio evolves. This self-similar evolution greatly simplifies our analysis as the formulation presented in preceding sections always applies to the bunch throughout the process, and the evolution is reduced to the determination of two degrees of freedom. Specifically, the temporal evolution of the entire bunch can be represented by the evolution of two unit-less scaling functions, $R(t)$ and $Z(t)$. Since these formulas hold, the trajectory of any particle

with initial positions (r_0, z_0) inside the uniform spheroid at a later time t can be expressed as by $(r_0 R(t), z_0 Z(t))$, where R and Z are independent of the arbitrary initial position (r_0, z_0). Thus, the parameters for describing the bunch change according to:

- the semi-axes of the spheroids as $(a, c) = (a_0 R, c_0 Z)$,

- the transient aspect ratio as $\alpha(t) = \alpha_0 \cdot \frac{R}{Z}$,

- the charge density from conservation of charge[3] as $\rho_c(t) = \frac{\rho_{c0}}{R^2 Z} = \frac{n_0 e}{R^2 Z}$,

- the longitudinal width as $\sigma_z^2(t) = \sigma_{z0}^2 \cdot Z^2$.

In the non-relativistic limit, each individual electron $[j]$ with initial position (r_0, z_0) follows the Newton's second law as:

$$\frac{d^2}{dt^2}(r_0 R) = \frac{e E_r(\alpha)}{m_e} = \frac{n_0 e^2}{2\varepsilon_0 m_e} \frac{\xi_r(\alpha)}{R^2 Z} \cdot (r_0 R) \tag{2.20a}$$

$$\frac{d^2}{dt^2}(z_0 Z) = \frac{e E_z(\alpha)}{m_e} = \frac{n_0 e^2}{2\varepsilon_0 m_e} \frac{\xi_z(\alpha)}{R^2 Z} \cdot (z_0 Z) \tag{2.20b}$$

Similarly, the bunch evolution then follows the equations of motion (EOM) in such an electric field, which can be reduced to the following two dimensionless ordinary differential equations (ODEs):

$$\frac{d^2 R}{d\tau^2} = \frac{\xi_r(\alpha)}{RZ} \tag{2.21a}$$

$$\frac{d^2 Z}{d\tau^2} = \frac{\xi_z(\alpha)}{R^2} \tag{2.21b}$$

---

[3] $N_{total} = \rho_{c0} \cdot (4\pi/3) a_0^2 c_0 = \rho_c(t) \cdot (4\pi/3) a^2 c$

with unit-less reduced time τ,

$$\tau = t \cdot \sqrt{\frac{e^2 n_0}{2\varepsilon_0 m_e}} = t \cdot \Omega_0 \tag{2.22}$$

initial electron number density n_0, and electron mass m_e. Notice that first, the time scaling factor $\Omega_0 = \frac{\omega_{p0}}{\sqrt{2}}$, where $\omega_{p0}(n_0) = \sqrt{\frac{e^2 n_0}{\varepsilon_0 m_e}}$ is the initial plasma frequency. Second, bear in mind that the geometry coefficients ξ_r and ξ_z are solely dependent on the transient aspect ratio α rather than specific values of a and c.

This means that starting with the same initial conditions for the ODE, bunches with the same initial aspect ratio α_0 but with different initial densities n_0, will have behaviors which only differ by the time scaling factor Ω_0 determined by the initial density n_0. The ones with higher density evolve faster, but the evolution trajectory reduces to the one with lower density after the evolution time is scaled according to the initial Ω_0.

2.1.3   Initial condition and Coulomb Explosion

We present the initial condition for solving uniform electron bunch evolution with the ODE described above. In order to achieve this, we rely on one particular example from Grech et al., [22], which begins with the initial conditions corresponding to a uniform spheroidal electron bunch expanding under the Coulomb force from rest, a phenomenon often referred to as Coulomb explosion.

According to the definition of the two scaling functions, we can have

$$R(\tau = 0) = 1 \tag{2.23a}$$

$$Z(\tau = 0) = 1 \tag{2.23b}$$

$$\left.\frac{dR}{d\tau}\right|_{\tau=0} = 0 \tag{2.23c}$$

$$\left.\frac{dZ}{d\tau}\right|_{\tau=0} = 0 \tag{2.23d}$$

Specifically, Eq.2.23a and Eq.2.23b represent the initial scaling of the spheroid and are by definition equal to 1. Meanwhile, Eq.2.23c and Eq.2.23d represent the initial change rate of the scaling function R and Z, or the initial velocity of the expansion. As the bunch starts from rest in this Coulomb explosion calculation, these rates equal to zero.

Using these initial conditions, the predictions derived from the ODEs (Eq. 2.21) are found to be in good agreement with molecular dynamics (MD) simulations for time-dependent energy distribution and particle-in-cell (PIC) simulations for temporal spheroid radii evolution [22, 29].

2.1.4 Critical Chirp ω_c^*, Crossover and Bounce-back

In addition to setting the initial velocity of the scaling faction (Eq.2.23c and Eq.2.23d) to zero for bunches starting from rest, we can also assign non-zero initial velocities,[4] for

---

[4]Instead of being any function of r or z

bunches start with initial linear chirp. For example, we can have initial velocities as:

$$\frac{dR}{d\tau}\bigg|_{\tau=0} = 0 \tag{2.24a}$$

$$\frac{dZ}{d\tau}\bigg|_{\tau=0} = \omega^* \tag{2.24b}$$

where ω^* is proportional to a longitudinal linear chirp. By linear chirp, we mean a linear correlation between momentum and position. Specifically, the linear chirp in MFT means that we are assuming for each individual particle, the longitudinal momentum p_z is proportional to its longitudinal position z.

The addition of this longitudinal linear chirp enables MFT to model bunches with a linear chirp in the longitudinal direction, such as the probing electron bunch after a longitudinal focusing lens, e.g. an RF cavity. As such, the initial momentum in the longitudinal direction of any electron $[j]$ with its longitudinal position $z[j]$ is expressed as:

$$p_z[j] = \mathcal{C}_z \cdot z[j] = m_e \cdot (\omega^* \Omega_0 \cdot z[j]) \tag{2.25}$$

where $\mathcal{C}_z$ is the actual linear chirp in simulations and experiments. We refer to ω^* as reduced linear chirp because it serves as a linear chirp in the dimensionless EOM and scales from the actual chirp in experiments only by Ω_0 as a result of the difference in the reduced time τ. If the initial reduced chirp is negative, Z will initially decrease, i.e. the bunch will be compressed in the longitudinal direction. As ω^* is proportional to the actual chirp via a parameter entirely dependent on density, we drop the "reduced" from ω_c^* when we refer to only the reduced chirp, but we keep the "reduced" when we are comparing the reduced chirp in the model with the actual chirp from the experiments and simulations.

The initial bunch density determines the time scale of the evolution. Therefore, the categorization of the focusing process of a uniformly charged spheroid is entirely determined by the initial reduced chirp and the initial aspect ratio. The effect of aspect ratio on bunch evolution has been well studied [22]. Therefore, we examine the impact of the reduced chirp on the bunch focusing process at a pre-specified initial aspect ratio, $\alpha_0 = \frac{10}{75}$.

We define the critical time, τ_c, as the time when the bunch reaches its minimum width, $min(\sigma_z^2)$ during the focusing process. As Eq. 2.21b is only dependent on $\frac{1}{R^2}$, which is finite throughout our investigation, Z can become zero at some point in the compression process if the initial chirp provides sufficient focusing power to overcome the repulsive Coulomb force. We call the smallest magnitude of the initial reduced chirp that is able to compress Z to zero (i.e. $min(\sigma_z^2) = 0$) the critical reduced chirp, ω_c^*. This critical reduced chirp is also unitless, just as all the other quantities in the EOM and the initial condition. That means uniform spheroidal bunches with the same aspect ratio share the same reduced critical chirp as we will discuss later in this section. The focusing process then falls into two categories characterized by whether $min(\sigma_z^2)$ reaches zero. As shown in Fig.2.1, for $\omega^* < \omega_c^*$, the longitudinal width of the bunch is never zero. However, there is a time at τ_c, at which the bunch size reaches a minimum during the compression process. When $\tau_c = 0$ then $\omega^* = 0$, and it increases with ω^* increasing. This trend continues until the critical reduced chirp is reached where the minimum width reaches zero and the corresponding critical time τ_c goes to infinity ($\tau_c \to \infty$). When compressed by a chirp that is larger than the critical chirp, the bunch will overcome the Coulomb repulsion and be compressed through a longitudinal crossover, as electrons starting from one side of the bunch cross the center of mass and then begin to continue moving on the other side without changing direction of motion. We refer to this type of process as the "cross-over" regime. In this regime, further increasing the chirp
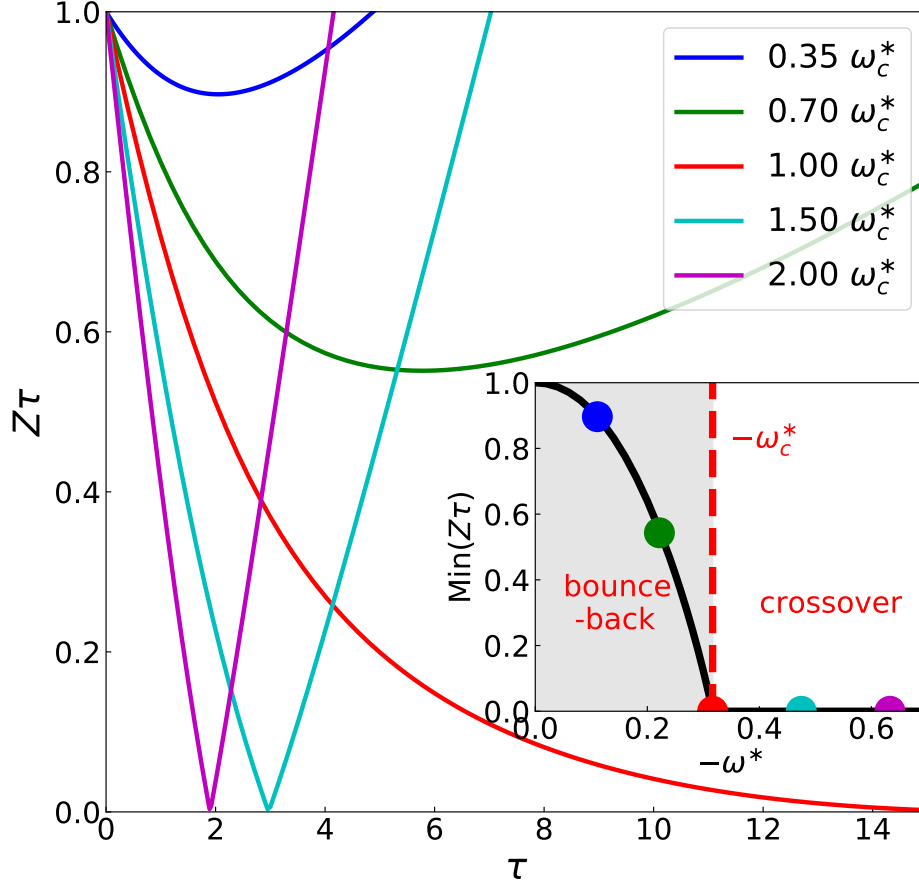
Figure 2.1: Longitudinal width evolution $Z(\tau)$ of prolate spheroids with ($\alpha_0 = 10/75$) driven by different initial chirps in numeric solutions of MFT ranging from below the critical chirp ($-0.35\omega_c^*$) to well above ($-2.0\omega_c^*$). The sub-graph shows the dependence of minimum width on initial reduced chirp. For this particular α_0, the critical value ω_c^* (red dot), divides the focusing into bounce-back and crossover regimes.

will decrease the critical time for the bunch to reach its minimum width, but the minimum width of the bunch during such compression will always be zero. In contrast, we call the regime below critical chirp the "bounce-back" regime as the particles follow trajectories that start out towards the center of mass and reverse their direction after the bunch reaches the minimum width, without any particle crossing.

The linearity of MFT (linear initial condition and linear self-field) indicates that for a bunch in the cross-over regime, all crossover incidents happen simultaneously across the entire bunch at the critical time (τ_c), creating a singularity in the EOM where the longitudinal

width goes to zero. To work through this singularity while numerically solving the EOM, we use a small time step to propagate the EOM until Z falls below zero. Then, we stop the calculation and flip the value of both the longitudinal position scaling, Z, and the longitudinal momentum, p_z to positive. The same EOM are then used to integrate the parameters for the expansion after crossover. In effect, this two-step process skips the singularity by infinitesimal step size in time. This two-step process is equivalent to assuming that the change of the bunch in the transverse direction is negligible during the infinitesimal time step around τ_c, which is validated by the fact that the transverse change rate or velocity is not divergent throughout the crossover. In addition, this two-step process also implies that in the cases where Z passes through zero, momentum does not change sign.

Analogous to the linear chirp we added in longitudinal direction, a radial chirp can also be introduced by altering the radial initial velocity in Eq.2.23c to a non-zero value. The linear chirp in the radial direction may be combined with the longitudinal chirp to model bunches compressed in both degrees of freedom simultaneously. However, in contrast to the longitudinal direction, MFT predicts that there is no such critical chirp in the radial direction. This occurs because the change in radial velocity is proportional to the inverse of R from Eq.2.21, which diverges as the bunch is compressed radially, preventing R from reaching zero. Compressing the bunch radially is equivalent to compressing the $\hat{x}$ and $\hat{y}$ simultaneously, and in this case there is only the bounce-back regime in the radial direction. Here, we focus on the longitudinal focusing where both bounce-back and cross-over regimes are accessible in MFT.

The (longitudinal) critical reduced chirp is an interesting concept that is important but new to the community. It is important because the bunch evolution is sensitive to emittance, especially when compressed by the critical chirp as we will show in next chapter. One

important feature of the critical reduced chirp ω_c^*, is its exclusive dependence on initial aspect ratio α_0, which stems from the governing EOM solely depending on the aspect ratio. In Fig. 2.2, we present the reduced critical chirp ω_c^* as a function of the initial aspect ratio
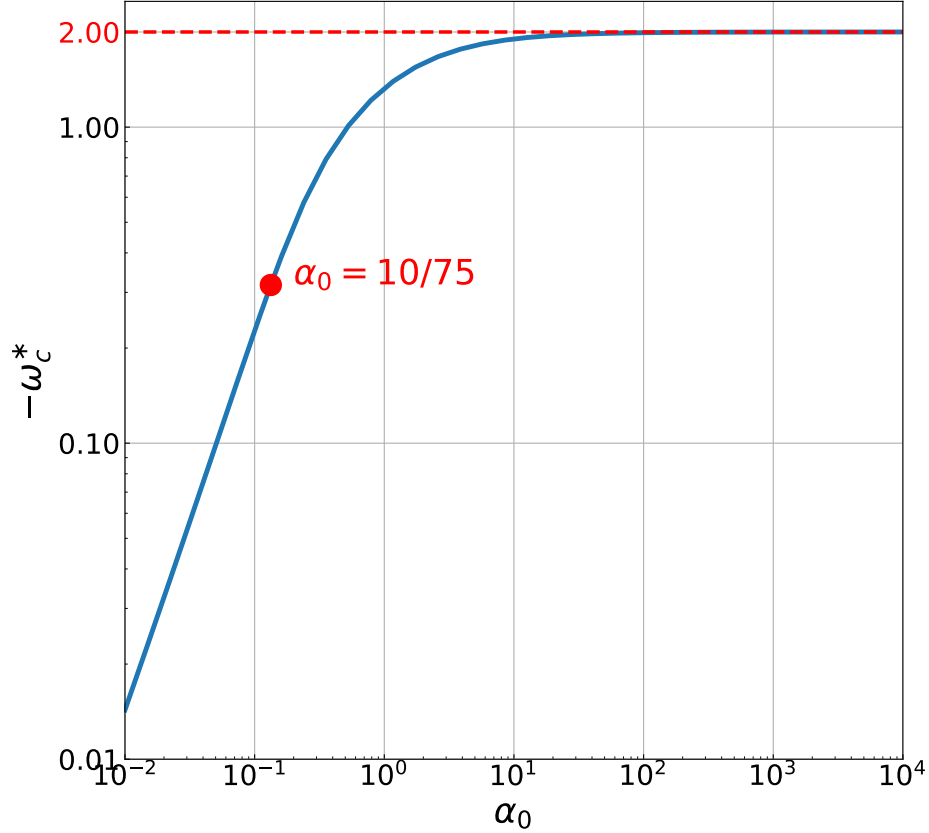
Figure 2.2: Dependence of critical reduced chirp ω_c^* on initial chirp α_0, with a horizontal asymptote of $\omega_c^*(\alpha_0 \to \infty) = 2$.

α_0. Specifically, note that for large α_0, we will always have $\alpha \gg 1$, where the geometry coefficients ξ_r and ξ_z in the EOM can be approximated in closed forms as [22]:

$$\xi_r(\alpha \to \infty) \simeq \frac{\pi}{2\alpha} \to 0 \tag{2.26a}$$

$$\xi_z(\alpha \to \infty) \simeq 2 - \frac{\pi\alpha^2}{(\alpha^2 - 1)^{3/2}} \to 2 \tag{2.26b}$$

The EOM reduces to the following:

$$R \simeq 1 \tag{2.27a}$$

$$\frac{d^2 Z}{d\tau^2} = 2 \tag{2.27b}$$

In other words, the trajectory of Z reduces to a constant acceleration. Therefore, the corresponding critical reduced chirp for large initial aspect ratio is simply:

$$Z(t) = Z_0 - \omega_c^* t + \frac{1}{2}\xi_z(\infty)t^2 \qquad \Rightarrow \qquad \omega_c^* = 2 \tag{2.28}$$

as we can see from Fig. 2.2.

2.2 Coulomb Potential inside a Gaussian Bunch

In addition to uniform bunches, researchers have been studying Gaussian density profiles of electron bunches [21] for various reasons. Gaussian bunches are appealing because the laser pulses generating the electrons from photo-cathodes generally have Gaussian profiles. In addition, the rich techniques available for Gaussian integrals provide a promising path toward a closed-form analytical model, which is also appealing to the theoretical community.

For the Gaussian bunch we are interested in, we assume that the charge density at point (x, y, z) depends on its scaling variable [37]:

$$\lambda(x, y, z) = \frac{x^2}{a^2} + \frac{y^2}{b^2} + \frac{z^2}{c^2} \tag{2.29}$$

where the semi-axes (a, b, c) equal the standard deviation of the entire bunch in each direction

$(\sigma_x, \sigma_y, \sigma_z)$. Then, the charge density profile can be expressed as a function of λ:

$$\rho(\lambda) = \rho(\frac{x^2}{a^2} + \frac{y^2}{b^2} + \frac{z^2}{c^2}) = \int d\lambda \cdot f(\lambda) \cdot \delta(\lambda - \frac{x^2}{a^2} - \frac{y^2}{b^2} - \frac{z^2}{c^2}) \qquad (2.30)$$

Accordingly, a Gaussian bunch can be modeled with:

$$f_G(\lambda) = \frac{Q}{\pi^{3/2} abc} e^{-\lambda} \qquad (2.31)$$

where Q is the total charge of the bunch. In other words, this bunch is constructed by a series of so-called homogeneous "scaled" shells, where the shells are bounded by ellipsoids with varying λ and the local volume charge density is the same within each shell with the value $f_G(\lambda)$.

We start with the contribution to the Coulomb potential from one single shell. We then integrate the contributions of each shell over the entire bunch yielding the Coulomb potential and field at any interior point of a Gaussian bunch. To conclude, we discuss the numerical strategy to model the Gaussian bunch evolution.

2.2.1   Potential Contribution from one single shell

We already have the potential for interior points $P(x, y, z)$ of a uniform ellipsoid of semi-axes (a, b, c) with density ρ_c from Eq. 2.12. Now, consider a similar ellipsoid of the same volume charge density ρ_c with scaled semi-axes $(\sqrt{\lambda}a, \sqrt{\lambda}b, \sqrt{\lambda}c)$. Accordingly, the surface of this scaled ellipsoid is defined by:

$$\frac{x^2}{a^2} + \frac{y^2}{b^2} + \frac{z^2}{c^2} = \lambda$$

We refer to this kind of arrangement as "similar and similarly placed" ellipsoids. Then, if E_{x2} is the x-component of the self field at $P(x, y, z)$ then,

$$E_{x2}(x, y, z) = x \cdot \frac{\rho_c abc}{2\varepsilon_0} \int_0^\infty \frac{\lambda^{3/2} ds}{(\lambda a^2 + s)\sqrt{(\lambda a^2 + s)(\lambda b^2 + s)(\lambda c^2 + s)}}. \qquad (2.32)$$

In this case, the integration variable can be substituted with $\tau = s/\lambda$, yielding the same electrostatic field as in Eq.2.17:

$$E_{x2}(x, y, z) = x \cdot \frac{\rho_c abc}{2\varepsilon_0} \int_0^\infty \frac{d\tau}{(a^2 + \tau)\sqrt{(a^2 + \tau)(b^2 + \tau)(c^2 + \tau)}} = E_x(x, y, z) \qquad (2.33)$$

and similarly, for E_{y2} and E_{z2}. Therefore, the field at any point of the vacuum space inside such homogeneous shell, which is bounded by two scaled and similarly placed ellipsoids, is zero. Meanwhile, if $\lambda > 1$, the potential in the hollow space has the constant value $V = (\lambda - 1)W$, where W is defined in Eq. 2.8.

If λ is very close but just slightly larger than 1, then the shell can be considered as a thin shell. Although the charge volume density is homogeneous within this thin shell, the surface charge density is not uniform, because the thickness is not a constant across the thin shell. The thickness of any point of the shell is proportional to the distance h from the center to the tangent plane at that point [38], which can be expressed as:

$$h(x, y, z) = \frac{\frac{x^2}{a^2} + \frac{y^2}{b^2} + \frac{z^2}{c^2}}{\sqrt{\frac{x^2}{a^4} + \frac{y^2}{b^4} + \frac{z^2}{c^4}}} = \frac{1}{\sqrt{\frac{x^2}{a^4} + \frac{y^2}{b^4} + \frac{z^2}{c^4}}} \qquad (2.34)$$

Therefore, the surface charge density on the shell reads:

$$\sigma(x, y, z) = \lim_{\lambda \to 1} \rho_c \cdot \left[(\lambda^{1/2} - 1) \cdot h(x, y, z) \right] = \lim_{d\lambda \to 0} \frac{\frac{1}{2} \cdot \rho_c \cdot d\lambda}{\sqrt{\frac{x^2}{a^4} + \frac{y^2}{b^4} + \frac{z^2}{c^4}}} \qquad (2.35)$$

Meanwhile, the surface charge density for a charged ellipsoidal conductor with the same semi-axes (a, b, c) shares the same form as:

$$\sigma = \frac{Q}{4\pi abc} \left(\frac{x^2}{a^4} + \frac{y^2}{b^4} + \frac{z^2}{c^4} \right)^{-\frac{1}{2}} \qquad (2.36)$$

with Q being the total charge on the conductor [38, 39]. The similarity in the surface charge distribution suggests that[5] we can use the existing potential and field expressions of a charged ellipsoidal conductor for our homogeneously charged thin shell. With a total charge Q_λ on the homogeneous thin shell λ in our Gaussian bunch[6] reads:

$$Q_\lambda = \lim_{d\lambda \to 0} \rho(\lambda) dV = 2\pi abc \cdot \lim_{d\lambda \to 0} \rho(\lambda) \lambda^{1/2} d\lambda \qquad (2.37)$$

Therefore, the contribution from any thin shell λ to the Coulomb potential at a point of interest $P_e(x_e, y_e, z_e)$ can be modeled as:

$$\phi_\lambda(x_e, y_e, z_e) = \begin{cases} \frac{1}{4\pi\varepsilon_0} \frac{Q_\lambda}{2} \int_\xi^\infty \frac{d\xi}{R_\lambda(\xi)} & \lambda_e \geq \lambda \\ \frac{1}{4\pi\varepsilon_0} \frac{Q_\lambda}{2} \int_0^\infty \frac{d\xi}{R_\lambda(\xi)} & \lambda_e < \lambda \end{cases} \qquad (2.38)$$

---

[5]In fact, the surface charge density on the ellipsoidal conductor is proportional to the fourth root of the total curvature of the surface. A detailed discussion can be found in [38]

[6]We are using the scaling variable λ of the inner surface of the shell from Eq.2.29 to designate each thin shell across our Gaussian bunch

with the corresponding $R_\lambda(\xi)$

$$R_\lambda(\xi) = \sqrt{(\lambda a^2 + \xi)(\lambda b^2 + \xi)(\lambda c^2 + \xi)} = \lambda^{3/2} R(\frac{\xi}{\lambda}) \tag{2.39}$$

and the lower limit of integration in ξ for exterior point cases comes from the largest root of the following equation:

$$\frac{x_e^2}{\lambda a^2 + \xi} + \frac{y_e^2}{\lambda b^2 + \xi} + \frac{z_e^2}{\lambda c^2 + \xi} = 1 \tag{2.40}$$

In other words, when the scaling variable λ_e of P_e:

$$\lambda_e = \lambda(x_e, y_e, z_e) = \frac{x_e^2}{a^2} + \frac{y_e^2}{b^2} + \frac{z_e^2}{c^2} \tag{2.41}$$

is larger than λ, the scaling factor of the thin shell, P_e is an exterior point and the lower limit of integration is the corresponding ξ from Eq.2.40. While if λ_e is smaller than λ, then P_e is an interior point and the lower limit of integration is zero.

2.2.2   Potential at an interior point of a Gaussian bunch

The potential at P_e due to the entire Gaussian bunch can be obtained by integrating the corresponding contribution over all the thin shells, as:

$$
\begin{aligned}
\phi(x_e, y_e, z_e) &= \sum \phi_{\lambda < \lambda_e} + \sum \phi_{\lambda > \lambda_e} \\
&= \frac{abc}{4\varepsilon_0} \int_0^{\lambda_e} \rho(\lambda)\lambda^{1/2} d\lambda \int_{\xi(\lambda)}^\infty \frac{d\xi}{R_\lambda(\xi)} + \frac{abc}{4\varepsilon_0} \int_{\lambda_e}^\infty \rho(\lambda)\lambda^{1/2} d\lambda \int_0^\infty \frac{d\xi}{R_\lambda(\xi)} \\
&= \frac{abc}{4\varepsilon_0} \int_0^\infty \rho(\lambda)\lambda^{1/2} d\lambda \int_{\xi(\lambda)}^\infty \frac{d\xi}{\lambda^{3/2} R(\xi/\lambda)} \\
&= \frac{abc}{4\varepsilon_0} \int_0^\infty \rho(\lambda) d\lambda \int_{t(\lambda)=\xi(\lambda)/\lambda}^\infty \frac{dt}{R(t)}
\end{aligned}
\tag{2.42}
$$

Here the relationship between t and λ for point P_e can be expressed as:

$$\lambda(x_e, y_e, z_e; t) = \frac{x_e^2}{a^2 + t} + \frac{y_e^2}{b^2 + t} + \frac{z_e^2}{c^2 + t} \tag{2.43}$$

derived from Eq. 2.40. The corresponding region of integration is shown as the colored area in Fig. 2.3.
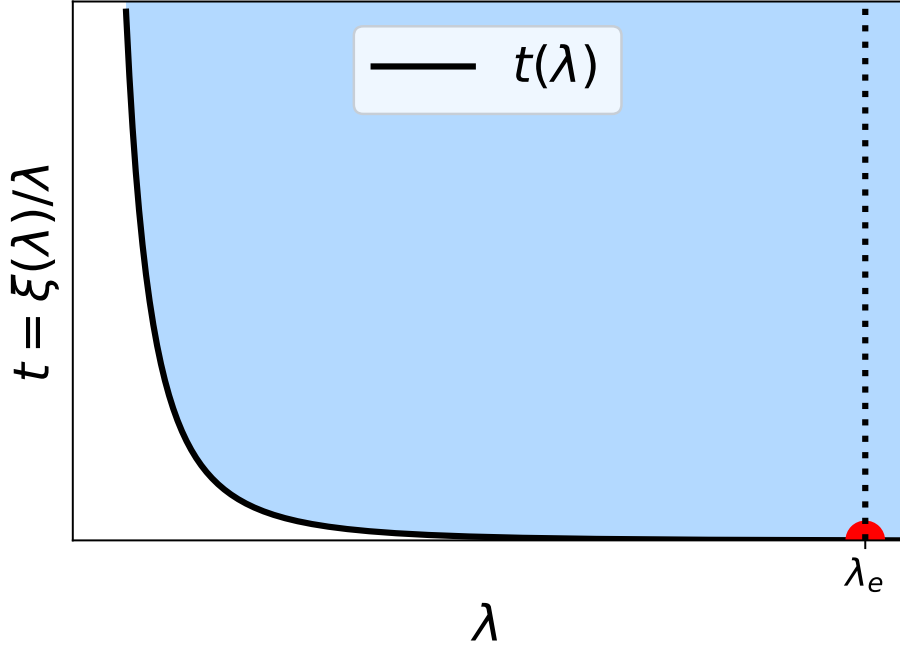
Figure 2.3: $t(\lambda)$ and integration region in blue. Notice that for $\lambda > \lambda_e$, we have $t = 0$ as P_e is an interior point of those shells

In order to take the advantage of our knowledge about the charge distribution function $\rho(\lambda)$, we interchange the order of integration:

$$\phi(x_e, y_e, z_e) = \frac{abc}{4\varepsilon_0} \int_0^\infty \rho(\lambda) d\lambda \int_{\xi(\lambda)/\lambda}^\infty \frac{dt}{R(t)} = \frac{abc}{4\varepsilon_0} \int_0^\infty \frac{dt}{R(t)} \int_{\lambda(t)}^\infty \rho(\lambda) d\lambda \tag{2.44}$$

assuming the potential is zero at infinity. If the potential is normalized such that the zero

point of the potential is at the center of the ellipsoid, then the potential can be written as:

$$\phi(x_e, y_e, z_e) = -\frac{abc}{4\varepsilon_0} \int_0^\infty \frac{dt}{R(t)} \int_0^{\lambda(t)} \rho(\lambda) d\lambda \tag{2.45}$$

For our Gaussian bunch, we insert the charge density profile as Eq. 2.31:

$$\rho(\lambda) = \frac{Q}{\pi^{3/2}abc} e^{-\lambda} \tag{2.46}$$

into Eq. 2.44. Therefore, the potential expression for an interior point of a Gaussian bunch reads:

$$\begin{aligned}
\phi(x_e, y_e, z_e) &= \frac{abc}{4\varepsilon_0} \frac{Q}{\pi^{3/2}abc} \int_0^\infty \frac{dt}{R(t)} \int_{\lambda(t)}^\infty e^{-\lambda} d\lambda \\
&= \frac{Q}{4\pi^{3/2}\varepsilon_0} \int_0^\infty \exp\left[-\frac{x_e^2}{a^2+t} - \frac{y_e^2}{b^2+t} - \frac{z_e^2}{c^2+t} \right] \frac{dt}{R(t)}
\end{aligned} \tag{2.47}$$

This expression is consistent with the existing literature [37]. In addition, the potential on an interior point of a uniform bunch in Eq. 2.12 can be reproduced as we take $\rho(\lambda)$ to a constant ρ_c in Eq. 2.45, with a trivial difference in the zero point of Coulomb potential. Since the only assumption involved is the ellipsoidal symmetry of the density profile (Eq. 2.30) with no restriction on the specific form of the density profile, this potential expression (Eq.2.44) is valid for bunches with same or higher symmetry like spherical and spheroidal symmetry.

Since the resulting electrostatic field from the Gaussian bunch is non-linear, it is not reasonable to apply the MFT formalism presented in the previous section for the evolution of a Gaussian bunch. A detailed discussion about this linearity assumption will be presented in the next section. Nevertheless, this potential and field formula from MFT will be useful

for our study when we apply statistical methods for the evolution of Gaussian bunches in the following chapter.

2.3   Discussion about the linearity assumption of MFT

The key assumption of the MFT formalism (Eq.2.21 as EOM with linear initial condition) is the linearity of the uniform bunch. This fundamental assumption stems from the linear self-field of uniform ellipsoidal bunches. The linearity of the entire system is maintained as long as the initial condition is also linear. Therefore, for MFT, the linearity assumption is equivalent to the self-similar evolution assumption, which greatly simplifies the expression of the uniform bunch evolution.

This linearity assumption is also one of the major limitations to MFT. Because of this, MFT cannot be applied to non-linear systems, such as the Gaussian bunch. Even if we divide the Gaussian bunch into scaled thin shells and treat them individually, the Gaussian bunch still drastically violates the linearity/self-similar evolution assumption of MFT, because its self-field is non-linear. Further complicating the situation, the non-linear field leads to different aspect ratios for shells across the bunch, which then breaks our scaled thin shell set-up for potential calculation in MFT.

Despite these limitations, MFT can be still be used to predict bunch evolution even when its assumptions are not strictly satisfied. When the assumptions are not fully met, the predictions will deviate from the actual evolution. The extent of this discrepancy depends on how far the bunch initial condition is from a uniform bunch with a perfect linear chirp used in MFT. A detailed discussion about the impact of different kinds of assumptions will be presented in the next chapter.

To reduce the limitations associated with linearity, we turn to statistical methods, which focus on the evolution of bunch statistics rather than the exact form of the density profile.

Chapter 3

Statistical Methods

In this chapter, we present statistical methods to model the evolution of electron bunches. We begin with an overview of the self-similar analytical (SSA) model for uniform ellipsoidal bunches. We then discuss the concept of emittance and its impact on bunch evolution by comparing SSA to MFT. To follow, we discuss a semi-statistical model for Gaussian bunches — the Analytic Gaussian (AG) model — to further illustrate the underlying assumptions of these statistical methods. We conclude this chapter by discussing the advantages and limitations of AG, SSA, and the equivalent Kapchinsky-Vladimirsky (KV) envelope equations.

3.1 The Self-similar Analytical Model

The SSA model, and other statistical methods, extract the bunch evolution trajectory directly from the time-derivatives of corresponding bunch statistics. We refer to these types of models as statistical methods. In contrast, the uniform bunch evolution in the MFT is found by integrating the uniform density profile with corresponding time-dependent parameters.

To properly introduce SSA and other statistical methods, we first discuss the dynamics of bunch statistics for a uniform ellipsoidal bunch. In each degree of freedom $i = T, z$, there are three second order statistics in the position-momentum phase space:[1] 1) the variance

---

[1] We are interested in second order statistics because of the definition of emittance. A detailed discussion will be presented in the Sec. 3.2

of the position σ_i^2, 2) the variance of the momentum $\sigma_{p_i}^2$, and 3) the correlation between position and momentum σ_{i,p_i}. Specifically, in the center of mass frame, we can have these three statistics:

$$\sigma_i^2 = \langle i^2 \rangle \tag{3.1a}$$

$$\sigma_{p_i}^2 = \langle p_i^2 \rangle \tag{3.1b}$$

$$\sigma_{i,p_i} = \langle i p_i \rangle \tag{3.1c}$$

where $i = x, y,$ or z and the $\langle \rangle$ operator yields the mean value, e.g. $\langle z p_z \rangle = \int \int z p_z f(r, p) dr dp$ for a continuous distribution in analytical models. We can

The non-relativistic evolution of the position and momentum can be written as:

$$i(t + dt) = i(t) + \frac{p_i(t)}{m} dt + \mathcal{O}(dt^2) \tag{3.2a}$$

$$p_i(t + dt) = p_i(t) + F_i(t) dt + \mathcal{O}(dt^2) \tag{3.2b}$$

with the force distribution function $F_i(t)$ based on the position information at time t. Therefore, the dynamics of these three statistics can be expressed as:

$$\frac{d\sigma_i^2}{dt} \simeq \frac{2}{m} \langle i p_i \rangle = \frac{2}{m} \sigma_{i,p_i} \tag{3.3a}$$

$$\frac{d\sigma_{p_i}^2}{dt} \simeq 2 \langle p_i F_i \rangle = 2 \sigma_{p_i, F_i} \tag{3.3b}$$

$$\frac{d\sigma_{i,p_i}}{dt} \simeq \langle i F_i + \frac{1}{m} p_i^2 \rangle = \sigma_{i,F_i} + \frac{1}{m} \sigma_{p_i}^2 \tag{3.3c}$$

We also have another set of three statistics specifically for SSA, which is equivalent to

Eq. 3.1, as follows:

$$\sigma_i^2 = \sigma_i^2 \tag{3.4a}$$

$$\gamma_i = \sigma_{i,p_i} \tag{3.4b}$$

$$\eta_i = \sigma_{p_i}^2 - \frac{\sigma_{i,p_i}^2}{\sigma_i^2} \tag{3.4c}$$

where η_i is the variance of local momentum fluctuations, the variance of the momentum after subtracting out the portion that is linearly correlated with position as shown below. A detailed definition[2] of these three statistics is illustrated in Fig. 3.1. In the longitudinal direction, σ_z^2 is the bunch spatial variance; γ_z is the correlation between the longitudinal position and momentum, and η_z is the variance of local momentum fluctuations in the longitudinal direction. Specifically, for each individual electron $[j]$, its longitudinal momentum $p_z[j]$ can be expressed as a linear function (with slope $\mathcal{C}_z$) of its longitudinal position $z[j]$ plus a random variable $\delta_z[j]$ as follows:

$$p_z[j] = \mathcal{C}_z \cdot z[j] + \delta_z[j] = \frac{\gamma_z}{\sigma_z^2} z[j] + \delta_z[j] \tag{3.5}$$

Here δ_z serves as the error term, with variance $\eta_z = \sigma_{\delta z}^2$. In addition, δ_z is assumed to be uncorrelated with the longitudinal position, i.e. $\sigma_{\delta_z,z} = 0$. With this set of notation, SSA essentially divides the variance of momentum into two parts: one part comes from the momentum which is linearly dependent on position of each particle and the other part is associated with the momentum that deviates from the linear part. The corresponding

---

[2]More underlying significance of these three statistics can be found in Sec. 3.3.1.
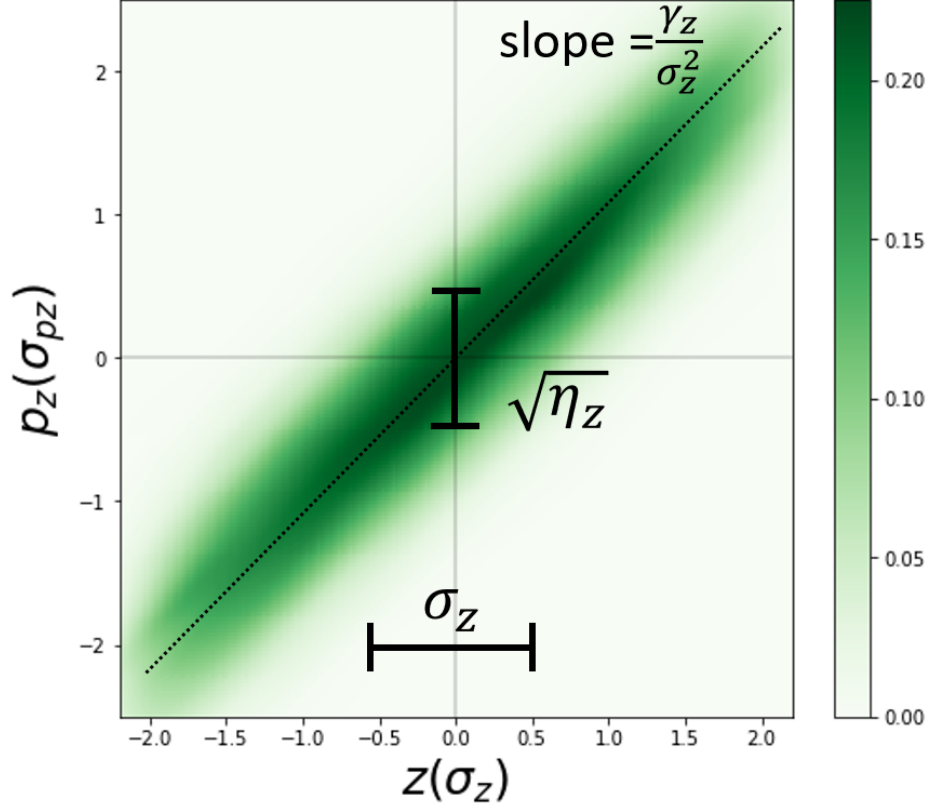
Figure 3.1: Schematic representation for the three bunch parameters in SSA

dynamics for SSA statistics can be derived from Eq. 3.3 as follows:

$$\frac{d\sigma_i^2}{dt} = \frac{2}{m}\gamma_i \tag{3.6a}$$

$$\frac{d\gamma_i}{dt} = \frac{1}{m}\left(\eta_i + \frac{\gamma_i^2}{\sigma_i^2}\right) + \sigma_{i,F_i} \tag{3.6b}$$

$$\frac{d\eta_i}{dt} = -\frac{2\gamma_i\eta_i}{m\sigma_i^2} + \frac{2}{\sigma_i^2}\left(\sigma_i^2\sigma_{p_i,F_i} - \sigma_{i,p_i}\sigma_{i,F_i}\right) \tag{3.6c}$$

The necessary initial conditions can be obtained by gathering the second-order statistics of

the bunch density distribution at the beginning of the evolution, namely the three bunch

statistics σ_i^2, γ_i, and η_i can be derived from the three direct second-order statistics of σ_i^2,

σ_{i,p_i}, and $\sigma_{p_i}^2$.

Coupled with proper force term, the SSA prediction of bunch evolution can be obtained

by numerically propagating the SSA dynamics from the initial conditions. Therefore, the key of SSA — that the bunch should evolve self-similarly — comes from the force distribution F_i. In other words, SSA assumes that the uniform ellipsoidal bunch will stay uniform while the density profile of a Gaussian bunch will stay as a Gaussian function. The self-similar evolution assumption simplifies the analysis by setting the force expression term F_i as the same form of function throughout the evolution with one (or more) time-dependent parameters in the charge density distribution.

For a uniform spheroidal bunch, as shown in Eq. 2.17, the electrostatic field is linearly dependent on the spatial position. In other words, the force term can be written as:

$$F_i = \frac{\rho_c e}{2\varepsilon_0} \cdot \xi_i(\alpha) \cdot i = \mathcal{K}_{Fi}(\alpha) \cdot i \tag{3.7}$$

where $i = T, z$ for the transverse[3] and longitudinal directions and α is the transient aspect ratio of the spheroid at time t. The corresponding second-order statistics related to F_i can then be simplified as:

$$\sigma_{i,F_i} = \mathcal{K}_{Fi}(\alpha) \cdot \sigma_i^2 \tag{3.8a}$$

$$\sigma_{p_i,F_i} = \mathcal{K}_{Fi}(\alpha) \cdot \sigma_{i,p_i} \tag{3.8b}$$

which also leads to the vanishing of the second term in Eq. 3.6c as:

$$\sigma_i^2 \sigma_{p_i,F_i} - \sigma_{i,p_i}\sigma_{i,F_i} = 0 \tag{3.9}$$

---

[3]As we take advantage of the rotational symmetry of spheroidal ellipsoids, the subscript T represents the two transverse directions, which includes both $\hat{x}$ and $\hat{y}$.

Therefore, the resulting SSA prediction of the self-similar evolution of a uniform spheroidal bunch yields:

$$\frac{d\sigma_i^2}{dt} = \frac{2}{m}\gamma_i \tag{3.10a}$$

$$\frac{d\gamma_i}{dt} = \frac{1}{m}\left(\frac{\gamma_i^2}{\sigma_i^2} + \eta_i\right) + \mathcal{K}_{Fi}(\alpha) \cdot \sigma_i^2 \tag{3.10b}$$

$$\frac{d\eta_i}{dt} = -\frac{2\gamma_i\eta_i}{m\sigma_i^2} \tag{3.10c}$$

One advantage of SSA is that the two-step process for dealing with the singularity at longitudinal crossover in MFT is not necessary here in the SSA model as the statistics themselves are second-order moments so that there is no need to flip the sign of spatial position and momentum in the cross-over regime.

Although the above derivations have been performed for Coulomb interactions, we would like to stress that the same conclusions can be drawn for any interaction that leads to linear dependence between force and position, such as gravitation [28]. Additionally, the generalization to any general ellipsoid is achieved by simply using three degrees of freedom with $i = X, Y, Z$ and corresponding geometry coefficients (ξ_x, ξ_y, ξ_z) with functions of the ratio between three axes $(\sigma_x : \sigma_y : \sigma_z)$.

3.2 Emittance and bunch evolution with conserved emittance

One of the major advantages of the SSA model (Eq. 3.10) is its inclusion of a conserved emittance, while MFT always assumes a zero-emittance bunch. In this analysis, we define

the "root-mean-square" (rms) emittance ε_i in each direction as:

$$\varepsilon_i^2 = \sigma_i^2 \sigma_{p_i}^2 - \sigma_{i,p_i}^2 = \sigma_i^2 \eta_i \tag{3.11}$$

This suggests that the value of emittance in each direction is proportional to the area of the contouring ellipse of the bunch in the 2D phase space regarding that direction. In other words, the rms emittance is not equal to the exact value of the occupied phase-space volume, but rather a statistical estimate of bunch phase-space volume based on the second-order statistics of the bunch. Although some literature conflates rms emittance with phase-space volume, these two concepts, while related, are not equal to each other. According to [40], emittance can grow while the actual phase-space volume stays constant as explained by Liouville's theorem.

To facilitate the analysis, we base our derivation using the square of emittance ε_i^2 which is the product of σ_i^2 and η_i. Thus, the evolution of squared emittance is:

$$\frac{d}{dt}\varepsilon_i^2 = \eta_i \frac{d}{dt}\sigma_i^2 + \sigma_i^2 \frac{d}{dt}\eta_i \tag{3.12}$$

Although, we use the squared emittance ε_i^2 for analytical derivations and discussions, we present results in emittance ε_i to ease the comparisons between model prediction and actual experiments.

As we look at the emittance evolution for uniform bunches, it is conserved within each degree of freedom according to Eq. 3.10, which seems to be the immediate result of the linear field/force assumption of Eq. 3.7. However, as we elaborate later in the next section, it is the linear chirp (self-similar evolution) assumption that ensures the conservation of emittance of

the bunch.

Additionally, if we take $\eta = 0$, (i.e. zero emittance), then the SSA model will reproduce the MFT, as shown in Fig.3.2. The linearity/self-similar evolution assumption is the reason why SSA, as a statistical method, can reproduce the result of MFT. The self-similar evolution assumption ensures the linearity across the bunch for SSA, as the linear momentum-position relationship in Eq. 3.5.

The emittance effect on the SSA dynamics can be explained by studying the evolution of the linear chirp $\mathcal{C}_i$ as we have:

$$\frac{d}{dt}\mathcal{C}_i = \frac{d}{dt}\left(\frac{\gamma_i}{\sigma_i^2}\right) = \mathcal{K}_{Fi}(\alpha) + \frac{\varepsilon_i^2}{m \cdot \left(\sigma_i^2\right)^2} \tag{3.13}$$

During the focusing process, the emittance term (last term in Eq. 3.13), will drive the negative chirp to approach zero faster. Therefore, the waist of the focusing process appears earlier than that predicted by MFT, resulting in a larger minimum width as well. Moreover, bigger emittance will lead to larger differences between predictions from SSA and MFT. These two emittance effects are also shown in Fig. 3.2.

3.3 Linear chirp assumption leads to conserved emittance

To further illustrate the fact that the linear chirp assumption conserves emittance in the SSA model, we provide the following derivation.

Although the electron bunches can have various density profiles, such as uniform or parabolic distributions, we start with an electron bunch with Gaussian density profile as an
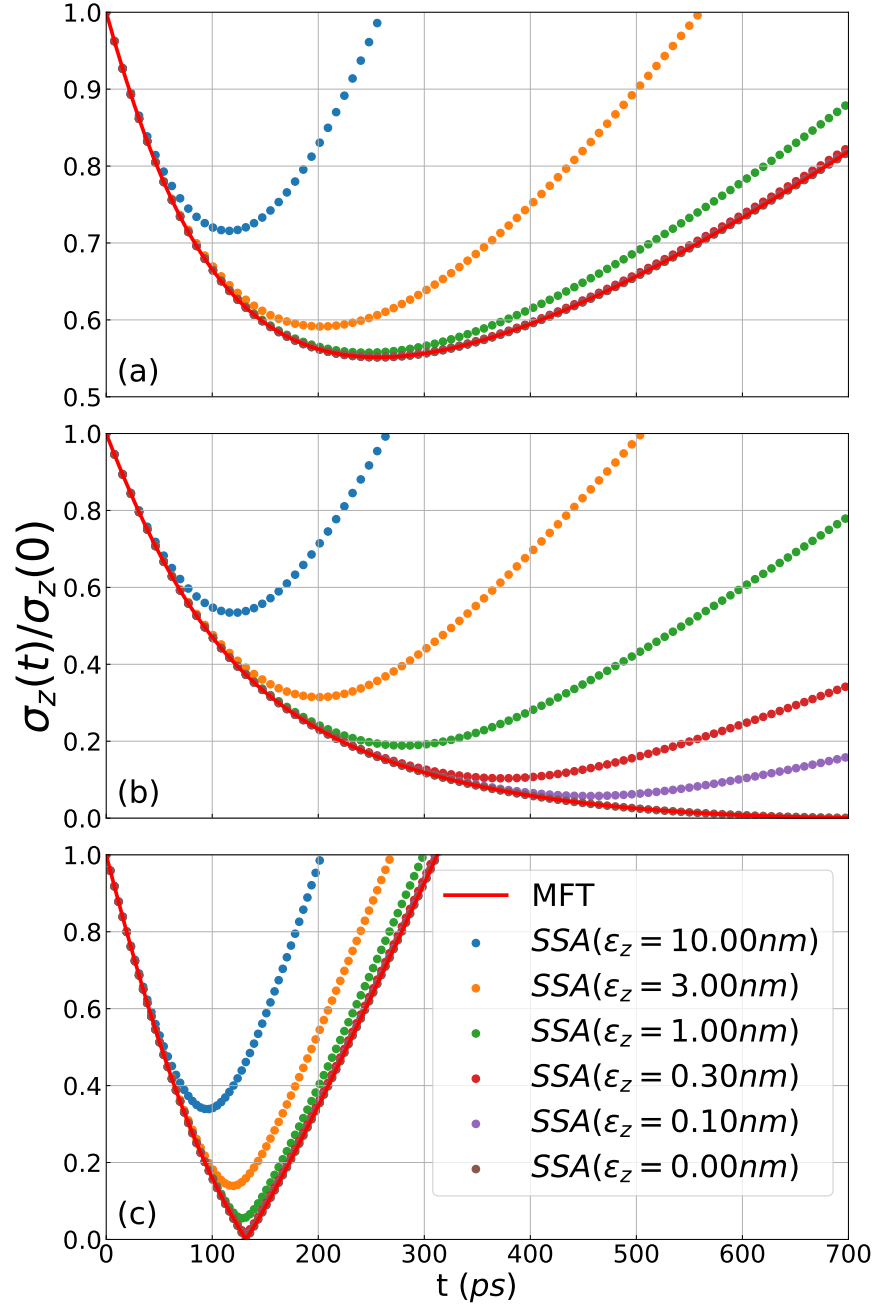
Figure 3.2: Longitudinal width evolution of prolate spheroids with ($\alpha_0 = 10/75$) focused by different initial chirps: (a) $0.7\omega_c^*$, (b)$1.0\omega_c^*$, (c) $1.5\omega_c^*$. In each figure, red solid line represents the prediction from MFT, dotted lines represent SSA with different emittance ranging from 0 to $0.01\mu m$ or $mm \cdot mrads$. The SSA with zero emittance and the MFT are in perfect agreement. Notice that (1) emittance move the waist larger and earlier comparing SSA and MFT, (2) comparing different chirps in SSA, the bunch evolution driven by critical chirp(b) shows higher sensitivity for emittance.

example. We rely on this example because the expression of the Gaussian density profile can have three explicit bunch statistics, the same set as in SSA, which makes it more advantageous for our analysis. The expression for the Gaussian density profile follows this general form:

$$f(r, p; t) = \mathcal{C}(t) \exp \left[\Sigma_i \left(\mathcal{G}_i(i) + \mathcal{H}_i(p_i, i) \right) \right] \tag{3.14}$$

where $i = x, y, z$. $\mathcal{G}_i$ is the function for the spatial distribution in each direction, which can be written as:

$$\mathcal{G}_i(i) = \frac{a_0 + a_2 i^2 + a_4 i^4 + \ldots + a_{2n-2} i^{2n-2} - a_{2n} i^{2n}}{2\sigma_i^2} \tag{3.15}$$

Meanwhile, $\mathcal{H}_i$ is the function for the momentum distribution, which can be written as:

$$\mathcal{H}_i(p_i, i) = -\frac{\left[p_i - \left(\gamma_i / \sigma_i^2 \right) i \right]^2}{2\eta_i} \tag{3.16}$$

where $(\sigma_i^2, \gamma_i, \eta_i)$ are the time-dependent statistical descriptions of the bunch in each direction we previously defined in SSA. The linear chirp of the bunch can still be described as Eq. 3.6, which leads to the self-similar evolution. The corresponding time derivative of squared emittance reads:

$$\frac{d}{dt} \varepsilon_z^2 = \eta_z \frac{d\sigma_z^2}{dt} + \sigma_z^2 \frac{d\eta_z}{dt} = 2 \left(\sigma_z^2 \sigma_{pz, Fz} - \sigma_{z, pz} \sigma_{z, Fz} \right) \tag{3.17}$$

3.3.1 The Linear chirp assumption in detail

In the proceeding section, I concluded that uniform ellipsoidal bunches conserve emittance after inserting the corresponding linear force from its self-field into the SSA model. Here I show that the linear chirp assumption also leads to conserved emittance, which is not

restricted to the uniform bunch density profile as a linear force assumption. The linear chirp assumption focuses on the statistical relationship between the spatial position and momentum for all the electrons of the bunch. Specifically, the linear chirp assumption assumes that the momentum of each individual electron j can be divided into two parts: the local average momentum based on the spatial position of electron j and the fluctuation part for electron j, just as we described in Eq. 3.5:

$$p_z[j] = \mathcal{C}_z \cdot z[j] + \delta_z[j] = \frac{\gamma_z}{\sigma_z^2} z[j] + \delta_z[j]$$

In the linear chirp assumption, the local average momentum is proportional to its spatial coordinates. That is, for longitudinal direction, the slope of this linear dependence (between local average momentum and spatial coordinate) $\mathcal{C}_z$ is decided by the two bunch statistics as $\frac{\gamma_z}{\sigma_z^2}$. Then, $\delta_z[j]$ is denoted as the difference between electron j's momentum and the projected local average momentum that is linearly based on its spatial coordinate, as shown in Eq. 3.5. We refer to δ_z as the local momentum fluctuation in the longitudinal direction with respect to the corresponding linear local average momentum. The variance of this local momentum fluctuation is then equal to η_z as we have:

$$
\begin{aligned}
\sigma_{p_z}^2 = \sigma_{\frac{\gamma_z}{\sigma_z^2} i + \delta_z}^2 &= \frac{\gamma_z^2}{\sigma_z^4} \sigma_z^2 + 2 \frac{\gamma_z}{\sigma_z^2} \sigma_{z,\delta_z} + \sigma_{\delta_z}^2 \\
&= \frac{\gamma_z^2}{\sigma_z^2} + \eta_z
\end{aligned}
\tag{3.18}
$$

with the assumption that δ_z and z are uncorrelated, i.e. $\sigma_{z,\delta_z} = 0$.

This assumption about δ_z and z being uncorrelated is the center piece for the linear chirp assumption. Because the linear local average momentum can always be projected to

the bunch density profile from the corresponding bunch statistics, the linear chirp assumption is essentially assuming the local momentum fluctuation with respect to that linear average momentum is uncorrelated with the spatial position. In other words, the momentum of electrons in bunches that do not satisfy that linear chirp assumption can still be expressed in Eq. 3.5, but the corresponding local momentum fluctuation (δ_i) will then be correlated with the spatial position. Therefore, the linear chirp assumption is actually focusing on the local momentum fluctuation (with respect to that linear chirp) being uncorrelated with the spatial position.

One possible expression of $\mathcal{H}$ in a Gaussian density profile that satisfies the linear chirp assumption is:

$$\mathcal{H}_z(p_z, z) = -\frac{1}{2\eta_z}\left[p_z - \frac{\gamma_z}{\sigma_z^2}z\right]^2 \tag{3.19}$$

which assumes that for any point inside the ellipsoidal bunch, the density distribution in momentum space with respect to the corresponding local average momentum has a Gaussian profile. The two bunch statistics involving p_z become:

$$\sigma_{p_z, F_z} = \sigma_{\frac{\gamma_z}{\sigma_z^2}z + \delta_z, F_z} = \frac{\gamma_z}{\sigma_z^2}\sigma_{z, F_z} + \sigma_{\delta_z, F_z} \tag{3.20a}$$

$$\sigma_{z, p_z} = \sigma_{z, \frac{\gamma_z}{\sigma_z}z + \delta_z} = \frac{\gamma_z}{\sigma_z}\sigma_z^2 + \sigma_{z, \delta_z} \tag{3.20b}$$

Accordingly, we can rewrite the evolution of emittance as:

$$\begin{aligned}\frac{d\varepsilon_z^2}{dt} &= 2\left[\sigma_z^2\left(\frac{\gamma_z}{\sigma_z}\sigma_{z, F_z} + \sigma_{\delta_z, F_z}\right) - \left(\frac{\gamma_z}{\sigma_z}\sigma_z^2 + \sigma_{z, \delta_z}\right)\sigma_{z, F_z}\right] \\ &= 2\left(\sigma_z^2\sigma_{\delta_z, F_z} - \sigma_{z, \delta_z}\sigma_{z, F_z}\right)\end{aligned} \tag{3.21}$$

The second term equals to zero as $\sigma_{z, \delta_z} = 0$ from the linear chirp assumption. The first term

also vanishes if the bunch density profile is symmetric with respect to the spatial position and fluctuation of momentum. Specifically, we can have:

$$\tilde{f}(z, \delta_z) = \tilde{f}(z, -\delta_z) = \tilde{f}(-z, \delta_z) \tag{3.22}$$

with $\tilde{f}$ being the shifted density distribution of the original one as:

$$\tilde{f}(z, \delta_z) = f(z, \frac{\gamma_z}{\sigma_z^2}z + \delta_z) = f\left(z, p_z(z, \delta_z)\right) \tag{3.23}$$

for a symmetric bunch density profile. The immediate consequence of a symmetric density distribution is that the magnitude of force due to the self-field can be expressed as an odd function of the spatial coordinates, i.e.

$$F_z(x, y, z) = -F_z(x, y, -z) \tag{3.24}$$

Then, the following covariance term related to the force distribution vanishes as:

$$\sigma_{\delta_z, F_z} = \int \int \delta_z F_z(z) \tilde{f}(z, \delta_z; t) dr dp \tag{3.25a}$$

Specifically, this covariance term vanishes when we pair $\delta_z F_z(z) \tilde{f}(z, \delta_z; t)$ and $\delta_z F_z(-z) \tilde{f}(-z, \delta_z; t)$ together, as these cancel each other out. As both terms in Eq. 3.21 equal to zero for a symmetric density profile, the emittance is conserved throughout the evolution, as:

$$\frac{d\varepsilon_z^2}{dt} = 0 \tag{3.26}$$

In addition, any symmetric density profile that satisfies Eq. 3.22 can lead to conserved emittance, not limited to the general Gaussian density profile mentioned at the beginning of this section.

As demonstrated throughout these derivations, it becomes clear that the exact form of the electron bunches' density profiles do not affect emittance conservation. As long as Eq. 3.22 is satisfied, the emittance is conserved. In other words, if the fluctuation of momentum δ_i of each individual electron is uncorrelated with its spatial position, the ellipsoidal symmetric bunch conserves emittance throughout its evolution.

3.3.2 A Comparison Between the SSA model and the Analytic Gaussian model

To further validate the argument that emittance conservation does not depend on the exact form of the spatial portion of the bunch's density profile, we overview the Analytic Gaussian (AG) model — a semi-statistical mean-field approach for bunch evolution with Gaussian density profiles.

Michalik and Sipe [30] introduced the AG model to study the evolution of bunch statistics with Gaussian profiles in both spatial and momentum space. Their key assumption is that bunches retain their Gaussian density profiles with the three time-dependent parameters in each direction. We generally base the following derivation on the original AG paper, however, we substitute in the SSA notation for consistency throughout this analysis.

We start with the Gaussian density profile used in the AG model:

$$f(\boldsymbol{r}, \boldsymbol{p}; t) = C(t) \exp[-\Gamma(\boldsymbol{r}, \boldsymbol{p}; t)] \tag{3.27}$$

with

$$\Gamma(\boldsymbol{r}, \boldsymbol{p}; t) = \frac{x^2 + y^2}{2\sigma_T^2} + \frac{[p_x - (\gamma_T/\sigma_T^2)x]^2 + [p_y - (\gamma_T/\sigma_T^2)y]^2}{2\eta_T}$$
$$+ \frac{z^2}{2\sigma_z^2} + \frac{[p_z - (\gamma_z/\sigma_z^2)z]^2}{2\eta_z} \tag{3.28}$$

This expression has three main assumptions. First, this expression assumes rotational symmetry in $\hat{x}$ and $\hat{y}$ direction. The subscript T then represents the two transverse directions, which includes both $\hat{x}$ and $\hat{y}$. The longitudinal direction is denoted with subscript $\hat{z}$. Second, the three bunch parameters in the AG model,[4] $(\sigma_z^2, \gamma_z, \eta_z)$ are the same as those used in the SSA model. This expression means the bunch has linear chirps in each direction and the momentum follows a relationship similar to Eq. 3.5, which is illustrated in Fig. 3.1 for the longitudinal direction. In other words, the Gaussian bunch in the AG model has linear chirp in each direction, with the corresponding momentum spread is uncorrelated with the spatial position. Therefore, the AG model is essentially modeling the longitudinal focusing of a spheroidal Gaussian bunch by calculating the self-similar evolution of a Gaussian bunch with the same initial bunch statistics. Third, the time-dependent normalization factor $C(t)$ comes from the conservation of total charge, which can be expressed as:

$$\int f(\boldsymbol{r}, \boldsymbol{p}; t) dr dp = N \quad \Rightarrow \quad C(t) = \frac{N}{(2\pi)^3} \left(\frac{1}{\sigma_T^2 \eta_T^2 \sigma_z \eta_z} \right)^{1/2} \tag{3.29}$$

That is, this density profile is a function of the three parameters in each direction (T and z). Therefore, the evolution of Gaussian bunches in the AG model can be generated from the trajectories of the three parameters of the bunch in each direction.

---

[4]We are illustrating the parameters for longitudinal direction. Similar notations apply to transverse direction as well.

By assuming the Gaussian bunch follows a self-similar evolution, the AG model allows researchers to model bunch evolution with Coulomb interactions in two main ways. First, the impact of the Coulomb interactions can be modeled by evaluating the corresponding Gaussian integrals. Specifically, the bunch evolution in each direction can be expressed by the trajectories of the three parameters in Eq.3.28. The resulting force terms in the time-derivatives of the bunch parameters are expressed as functions of the transient aspect ratio ($\alpha(t) = \sigma_T/\sigma_z$). Second, because the bunch retains a Gaussian profile, the AG model captures the Coulomb effect throughout the evolution of the electron bunch. Specifically, this can be expressed using the same force term with the time-dependent aspect ratio. These two advantages of the AG model make the theoretical expression of the bunch evolution with Coulomb interaction feasible assuming a self-similar Gaussian bunch.

The pathway to the force term is a two-step process. First, we calculate the three parameters of the Gaussian density profile $f(\boldsymbol{r}, \boldsymbol{p}; t)$ to calculate the Coulomb effect on the bunch emittance evolution. Second, we integrate over the "flow" term and "force" term from the time derivative of f to eventually solve for the time derivative of these three parameters. Specifically, for the longitudinal direction,[5] we have:

$$\sigma_z^2 = \frac{1}{N} \int z^2 f(\boldsymbol{r}, \boldsymbol{p}; t) d\boldsymbol{r} d\boldsymbol{p} = \mathcal{X}_{55} \tag{3.30a}$$

$$\gamma_z = \frac{1}{N} \int z p_z f(\boldsymbol{r}, \boldsymbol{p}; t) d\boldsymbol{r} d\boldsymbol{p} = \mathcal{X}_{56} \tag{3.30b}$$

$$\eta_z + \frac{\gamma_z^2}{\sigma_z^2} = \frac{1}{N} \int p_z^2 f(\boldsymbol{r}, \boldsymbol{p}; t) d\boldsymbol{r} d\boldsymbol{p} = \mathcal{X}_{66} \tag{3.30c}$$

Here we use $\mathcal{X}_{ij}$ to represent the corresponding second moment of the Gaussian profile

---

[5]Similar results can be applied to the transverse direction for both $\hat{x}$ and $\hat{y}$.

$f(\boldsymbol{r}, \boldsymbol{p}; t)$ for simplicity. That is:

$$\mathcal{X}_{ij} = \frac{1}{N} \int u_i u_j f(\boldsymbol{r}, \boldsymbol{p}; t) d\boldsymbol{r} d\boldsymbol{p} \tag{3.31}$$

with $(u_1, u_2, u_3, u_4, u_5, u_6) = (x, p_x, y, p_y, z, p_z)$. Conveniently, we can have the time derivative of $\mathcal{X}_{ij}$ as:

$$\frac{\partial}{\partial t} \mathcal{X}_{ij} = \frac{1}{N} \int u_i u_j \frac{\partial f(\boldsymbol{r}, \boldsymbol{p}; t)}{\partial t} d\boldsymbol{r} d\boldsymbol{p} \tag{3.32}$$

Therefore, the time derivatives of the three parameters can be written as:

$$\frac{\partial}{\partial t} \sigma_z^2 = \frac{1}{N} \int z^2 \frac{\partial f(\boldsymbol{r}, \boldsymbol{p}; t)}{\partial t} d\boldsymbol{r} d\boldsymbol{p} = \frac{\partial}{\partial t} \mathcal{X}_{55} \tag{3.33a}$$

$$\frac{\partial}{\partial t} \gamma_z = \frac{1}{N} \int z p_z \frac{\partial f(\boldsymbol{r}, \boldsymbol{p}; t)}{\partial t} d\boldsymbol{r} d\boldsymbol{p} = \frac{\partial}{\partial t} \mathcal{X}_{56} \tag{3.33b}$$

$$\frac{\partial}{\partial t} \eta_z = -\frac{2\gamma_z}{\sigma_z^2} \frac{\partial}{\partial t} \gamma_z + \frac{\gamma_z^2}{(\sigma_z^2)^2} \frac{\partial}{\partial t} \sigma_z^2 + \frac{1}{N} \int p_z^2 \frac{\partial f(\boldsymbol{r}, \boldsymbol{p}; t)}{\partial t} d\boldsymbol{r} d\boldsymbol{p}$$

$$= \left(\frac{\gamma_z}{\sigma_z^2}\right)^2 \frac{\partial}{\partial t} \mathcal{X}_{55} - 2\frac{\gamma_z}{\sigma_z^2} \frac{\partial}{\partial t} \mathcal{X}_{56} + \frac{\partial}{\partial t} \mathcal{X}_{66} \tag{3.33c}$$

According to the Vlasov equation, we can rewrite $\partial f / \partial t$ as:

$$\frac{\partial f(\boldsymbol{r}, \boldsymbol{p}; t)}{\partial t} = -\frac{\partial f(\boldsymbol{r}, \boldsymbol{p}; t)}{\partial r} \frac{\partial r}{\partial t} - \frac{\partial f(\boldsymbol{r}, \boldsymbol{p}; t)}{\partial p} \frac{\partial p}{\partial t}$$

$$= \left(-\frac{p}{m}\right) \frac{\partial f(\boldsymbol{r}, \boldsymbol{p}; t)}{\partial r} - \frac{\partial f(\boldsymbol{r}, \boldsymbol{p}; t)}{\partial p} F(r) \tag{3.34}$$

The integral of the first term is called the "flow" term, K_{ij}^{flow}, as it comes from fundamental kinematics. The integral of the second term is called the "force" term, K_{ij}^{force}. The force term represents the effect of the Coulomb interaction on the bunch evolution.

Accordingly, we rewrite Eq.3.32 as:

$$
\frac{\partial}{\partial t}\mathcal{X}_{ij} = \frac{1}{N}\int u_i u_j \frac{\partial f(r,p;t)}{\partial t}d\boldsymbol{r}d\boldsymbol{p}
$$

$$
= \frac{1}{N}\int u_i u_j \left(-\frac{p}{m}\right)\frac{\partial f(r,p;t)}{\partial r}d\boldsymbol{r}d\boldsymbol{p} + \frac{1}{N}\int u_i u_j \left(-\frac{\partial f(r,p;t)}{\partial p}\right)F(r)d\boldsymbol{r}d\boldsymbol{p} \quad (3.35)
$$

$$
= K_{ij}^{flow} + K_{ij}^{force}
$$

We start with the flow term. The spatial derivative of the Gaussian density profile f is:

$$
\frac{\partial f(r,p;t)}{\partial z} = \left[\frac{1}{\sigma_z^2}z - \frac{\gamma_z}{\sigma_z^2\eta_z}\left(p_z - \frac{\gamma_z}{\sigma_z^2}z\right)\right]f(r,p;t)
$$

$$
= \left[\left(\frac{1}{\sigma_z^2} + \frac{\gamma_z^2}{\sigma_z^4\eta_z}\right)z - \frac{\gamma_z}{\sigma_z^2\eta_z}p_z\right]f(r,p;t)
$$

$$(3.36)$$

Therefore, the corresponding flow terms are:

$$
K_{55}^{flow} = \frac{1}{Nm}\int\int z^2 p_z \left[\left(\frac{1}{\sigma_z^2} + \frac{\gamma_z^2}{\sigma_z^4\eta_z}\right)z - \frac{\gamma_z}{\sigma_z^2\eta_z}p_z\right]f(r,p;t)drdp = \frac{2}{m}\gamma_z \quad (3.37a)
$$

$$
K_{56}^{flow} = \frac{1}{Nm}\int\int zp_z^2 \left[\left(\frac{1}{\sigma_z^2} + \frac{\gamma_z^2}{\sigma_z^4\eta_z}\right)z - \frac{\gamma_z}{\sigma_z^2\eta_z}p_z\right]f(r,p;t)drdp = \frac{1}{m}\left(\eta_z + \frac{\gamma_z^2}{\sigma_z^2}\right)
$$

$$(3.37b)$$

$$
K_{66}^{flow} = \frac{1}{Nm}\int\int p_z^3 \left[\left(\frac{1}{\sigma_z^2} + \frac{\gamma_z^2}{\sigma_z^4\eta_z}\right)z - \frac{\gamma_z}{\sigma_z^2\eta_z}p_z\right]f(r,p;t)drdp = 0 \quad (3.37c)
$$

If we assume $F(\boldsymbol{r}) = 0$, then the time derivatives of the three parameters (Eq. 3.33), with the effect of the flow term alone, models the evolution of a non-interacting bunch with a Gaussian density profile as Eq. 3.28. That is, the non-interacting bunch evolution could be

described by inserting Eq. 3.37 in the Eq. 3.33 as:

$$\frac{d\sigma_z^2}{dt} = \frac{2}{m}\gamma_z \tag{3.38a}$$

$$\frac{d\gamma_z}{dt} = \frac{1}{m}\left(\eta_z + \frac{\gamma_z^2}{\sigma_z^2}\right) \tag{3.38b}$$

$$\frac{d\eta_z}{dt} = -\frac{2\gamma_z\eta_z}{m\sigma_z^2} \tag{3.38c}$$

Since the three bunch statistics are only functions of time, we replace the partial derivatives with the total derivatives here to obtain the ordinary differential equation for the bunch statistics evolution. Unsurprisingly, the non-interacting bunch conserves emittance throughout the evolution when we insert Eq.3.38 into Eq.3.12.

For the purpose of measuring the Coulomb interaction effect on bunch evolution, especially on emittance conservation, we insert the corresponding force expression $F(\boldsymbol{r})$ derived from the expression of Coulomb potential, which we derived earlier (Eq.2.47). Consequently, the time derivative of the three parameters (Eq. 3.33) yields the collective effect of a Gaussian bunch through K_{ij}^{force}.

Specifically, the field distribution can be derived from Eq. 2.47 as:

$$E_z(x, y, z) = \frac{Q}{4\pi^{3/2}\varepsilon_0} \int_0^\infty \frac{2z}{c^2 + l} \cdot \frac{\exp\left[-\frac{x^2}{a^2+l} - \frac{y^2}{b^2+l} - \frac{z^2}{c^2+l}\right]}{\sqrt{(a^2 + l)(b^2 + l)(c^2 + l)}} dl \tag{3.39}$$

By leveraging the following substitutions:

$$\mathcal{K} = \frac{Qe}{2\pi^{3/2}\varepsilon_0} \tag{3.40a}$$

$$R(l) = \sqrt{(a^2 + l)(b^2 + l)(c^2 + l)} \tag{3.40b}$$

$$\lambda(x, y, z; l) = \frac{x^2}{a^2 + l} + \frac{y^2}{b^2 + l} + \frac{z^2}{c^2 + l} \tag{3.40c}$$

$$\mathcal{I}_c(x, y, z) = \int_0^\infty \frac{\exp\left[-\lambda(x, y, z; l)\right]}{(c^2 + l)R(l)} dl \tag{3.40d}$$

we can have a concise expression for the Coulomb force as:

$$F_z(x, y, z) = z \cdot \mathcal{K} \cdot \mathcal{I}_c(x, y, z) \tag{3.41}$$

Then, knowing that the derivative of f with respect to p_z is

$$\frac{\partial}{\partial p_z} f(r, p; t) = \frac{1}{\eta_z} \left(p_z - \frac{\gamma_z}{\sigma_z} z \right) f(r, p; t) \tag{3.42}$$

the force term in the longitudinal direction can be expressed as:

$$K_{55}^{force} = -\frac{1}{N\eta_z} \int \int z^3 \left(p_z - \frac{\gamma_z}{\sigma_z^2} z \right) \cdot \mathcal{I}_c(x, y, z) \cdot f(r, p; t) dr dp \tag{3.43a}$$

$$K_{56}^{force} = -\frac{1}{N\eta_z} \int \int z^2 p_z \left(p_z - \frac{\gamma_z}{\sigma_z^2} z \right) \cdot \mathcal{I}_c(x, y, z) \cdot f(r, p; t) dr dp \tag{3.43b}$$

$$K_{66}^{force} = -\frac{1}{N\eta_z} \int \int z p_z^2 \left(p_z - \frac{\gamma_z}{\sigma_z^2} z \right) \cdot \mathcal{I}_c(x, y, z) \cdot f(r, p; t) dr dp \tag{3.43c}$$

For the emittance evolution, we can insert Eq. 3.33 into Eq. 3.12 as:

$$
\begin{aligned}
\frac{d\varepsilon_z^2}{dt} &= \eta_z \frac{d\sigma_z^2}{dt} + \sigma_z^2 \frac{d\eta_z}{dt} \\
&= \left(\eta_z + \frac{\gamma_z^2}{\sigma_z^2} \right) K_{55}^{force} + \sigma_z^2 \left(K_{66}^{force} - \frac{2\gamma_z}{\sigma_z^2} K_{56}^{force} \right)
\end{aligned}
\tag{3.44}
$$

Thus the emittance evolution with Eq. 3.43:

$$
\frac{d\varepsilon_z^2}{dt} = -\frac{1}{N} \int \int \left[z^3 \left(p_z - \frac{\gamma_z}{\sigma_z^2} z \right) + \frac{\sigma_z^2}{\eta_z} z \left(p_z - \frac{\gamma_z}{\sigma_z^2} z \right)^3 \right] \cdot \mathcal{I}_c(x, y, z) \cdot f(r, p; t) dr dp \tag{3.45}
$$

We can simplify this expression by a simple substitution of variable as:

$$
\delta_z = p_z - \frac{\gamma_z}{\sigma_z^2} z \tag{3.46}
$$

with the corresponding Jacobian:

$$
\mathcal{J} = \det \begin{bmatrix} 1 & 0 \\ -\frac{\gamma_z}{\sigma_z^2} & 1 \end{bmatrix} = 1 \tag{3.47}
$$

Accordingly, the density distribution function $f(r, p; t)$ shifts to $\tilde{f}$ as shown in Eq. 3.23. We can rewrite the time derivative of ε_z^2 as:

$$
\frac{d\varepsilon_z^2}{dt} = -\frac{1}{N} \int \int \left[z^3 \delta_z + \frac{\sigma_z^2}{\eta_z} z \delta_z^3 \right] \cdot \mathcal{I}_c(x, y, z) \cdot \tilde{f}(r, \delta_r; t) dr d\delta_r \tag{3.48}
$$

Since $\mathcal{I}_c(x, y, z)$ and $\tilde{f}$ are both even functions, this integral equals zero as we properly pair

the elements as expressed below:

$$(z, \delta_z) \qquad \text{and} \qquad (-z, \delta_z) \tag{3.49}$$

Therefore, emittance is conserved during the evolution of a Gaussian bunch according to the AG model, even with a non-linear self-field/force. This is consistent with what we argued in the proceeding section, that the linear chirp is the key assumption for conserved emittance, not the linear force.

We continue the derivation for the Coulomb effect on bunch evolution in the AG model. To further simplify the expression, we introduce the "bar" notation ($\overline{\mathcal{M}_z}$, $\mathcal{M}_z$ as a placeholder for the corresponding quantities, which will be evaluated for the longitudinal direction) as:

$$\overline{\mathcal{M}_z} = -\frac{1}{N\eta_z} \int \int \mathcal{M}_z \cdot \mathcal{I}_c(x, y, z) \cdot \tilde{f}(r, \delta_r; t) dr d\delta_r \tag{3.50}$$

Thus, we can rewrite the force term in Eq. 3.43 as

$$K_{55}^{force} = \overline{z^3 \delta_z} = 0 \tag{3.51a}$$

$$K_{56}^{force} = \overline{z^2 \delta_z \left(\delta_z + \frac{\gamma_z}{\sigma_z^2} z \right)} = \overline{z^2 \delta_z^2} + \frac{\gamma_z}{\sigma_z^2} \overline{z^3 \delta_z} = \overline{z^2 \delta_z^2} \tag{3.51b}$$

$$K_{66}^{force} = \overline{z \delta_z \left(\delta_z + \frac{\gamma_z}{\sigma_z^2} z \right)^2} = \overline{z \delta_z^3} + 2\frac{\gamma_z}{\sigma_z^2} \overline{z^2 \delta_z^2} + \left(\frac{\gamma_z}{\sigma_z^2} \right)^2 \overline{z^3 \delta_z} = 2\frac{\gamma_z}{\sigma_z^2} \overline{z^2 \delta_z^2} = \frac{2\gamma_z}{\sigma_z^2} K_{56}^{force} \tag{3.51c}$$

where the integrals of $z^3 \delta_z$ and $z \delta_z^3$ vanish due to the symmetry of $\mathcal{I}_c(x, y, z)$ and $\tilde{f}(r, \delta_r; t)$

(i.e. $f(r, p; t)$). As we can have a closed form $\overline{z^2 \delta_z^2}$ and similarly for $\overline{x^2 \delta_x^2}$ and $\overline{y^2 \delta_y^2}$:

$$K_{56}^{force} = \frac{1}{4\pi\epsilon_0} \frac{Ne^2}{6\sqrt{\pi}} \frac{1}{\sigma_z} L_z \left(\frac{1}{\alpha} \right) \tag{3.52a}$$

$$K_{12}^{force} = K_{34}^{force} = \frac{1}{4\pi\epsilon_0} \frac{Ne^2}{6\sqrt{\pi}} \frac{1}{\sigma_T} L_T \left(\frac{1}{\alpha} \right) \tag{3.52b}$$

where $L_i(p)$ is:

$$L_z(p) = \frac{3p^2}{p^2 - 1} [pL(p) - 1] \tag{3.53a}$$

$$L_T(p) = \frac{3}{2} \left[L(p) + \frac{p^2 L(p) - p}{1 - p^2} \right] \tag{3.53b}$$

and $L(p)$ as:

$$L(p) = \frac{1}{2} \int_0^\pi \frac{d\theta}{1 + p\sin\theta} = \begin{cases} \dfrac{\arcsin\sqrt{1-p^2}}{\sqrt{1-p^2}}, & 0 \le p \le 1 \quad (oblate) \\[3ex] \dfrac{\ln(p+\sqrt{p^2-1})}{\sqrt{p^2-1}}, & 1 \le p \quad (prolate) \end{cases} \tag{3.54}$$

Once the flow term and force term are known, we can write the dynamics expression for the self-similar evolution of a Gaussian bunch with the three parameters:

$$\frac{d\sigma_i^2}{dt} = \frac{2}{m} \gamma_i \tag{3.55a}$$

$$\frac{d\gamma_i}{dt} = \frac{1}{m} \left(\eta_i + \frac{\gamma_i^2}{\sigma_i^2} \right) + \frac{1}{4\pi\epsilon_0} \frac{Ne^2}{6\sqrt{\pi}} \frac{1}{\sigma_i} L_i \left(\frac{1}{\alpha} \right) \tag{3.55b}$$

$$\frac{d\eta_i}{dt} = -\frac{2\gamma_i \eta_i}{m\sigma_i^2} \tag{3.55c}$$

55

3.3.3 Discussion about AG

The essence of the AG model is the evolution of a self-similar Gaussian bunch, where the chirp is linear and the local momentum fluctuation is uncorrelated with the electron's spatial position. It uses the initial bunch statistics as the initial values of the three time-dependent parameters of the Gaussian profile. Therefore, the credibility of AG's prediction comes down to the similarity between the actual charge density profile and the Gaussian profile that shares the same bunch statistics. This is the reason behind the good performance for the AG model, despite the fact that a Gaussian charge distribution does not evolve self-similarly [17,32].

To this extent, the AG model can be considered as an intermediate approach, which shifts the focus from the exact density profile towards bunch statistics. In other words, the advantage of the AG model is that it starts to focus more on the evolution of bunch statistics. However, the AG model is limited in that is assumes that bunches have and retain a Gaussian form.

3.4 Discussion

We presented the SSA model, a statistical method describing the second order moments to model the evolution of an ellipsoidal electron bunch and explained how it can reproduce the MFT by taking a zero momentum spread. We also discussed the linear chirp assumption, explaining how it is the key assumption to yield emittance conservation during the bunch evolution. In addition, we also shed light on the statistical nature of emittance, noting how the force impacts from the uniform density profile and Gaussian profile are similar to each other. In the following subsections, we expand our discussion upon all of these points.

3.4.1 linear chirp and self-similar evolution assumptions

The derivation outlined in the preceding section of this chapter showed that the key assumption for conserving emittance is the linear chirp assumption. In particular, the linear local average momentum can always be projected on the bunch distribution function by inserting the corresponding statistics into Eq. 3.5. The fluctuation of momentum (δ_i) is then the crucial quantity that differentiates bunches from conserving emittance or not. Just as we mentioned in the discussion about the MFT, if δ_i is not symmetric, or not uncorrelated with the spatial position, we can still use the SSA model or the AG model to estimate the evolution. However, these model estimations will deviate from the true evolution. In the next chapter, we explore the magnitude of this discrepancy.

We refer to the SSA model as the self-similar analytic model to differentiate it from the AG model. Specifically, through this naming, we emphasize the self-similar evolution assumption rather than the Gaussian density profile. In this analysis, the self-similar bunch evolution is also considered satisfying the linear chirp assumption throughout the evolution as this ensures that the bunch with a linear chirp will evolve self-similarly.[6] In reality, the Gaussian bunch generally does not evolve self-similarly, as pointed out by the literature [17, 32] as is also demonstrated in the simulation in the following section. Indeed, only uniform bunches with zero emittance evolve truly self-similarly.

---

[6]There will be edge effect due to the fluctuation of momentum that create density tails on the bunch edges, which means the bunch evolution is not strictly self-similar. We present a detailed discussion in the following section.

3.4.2 Kinetic energy transfer between degrees of freedom

The kinetic energy statistics of the bunch in each degree of freedom is related to the three statistics through:

$$KE_i = \frac{N}{2m}\sigma_{p_i}^2 = \frac{N}{2m}\left(\eta_i + \frac{\gamma_i^2}{\sigma_i^2}\right) \tag{3.56}$$

The corresponding result of a crossover case is shown in Fig.3.3 The kinetic energy evolution
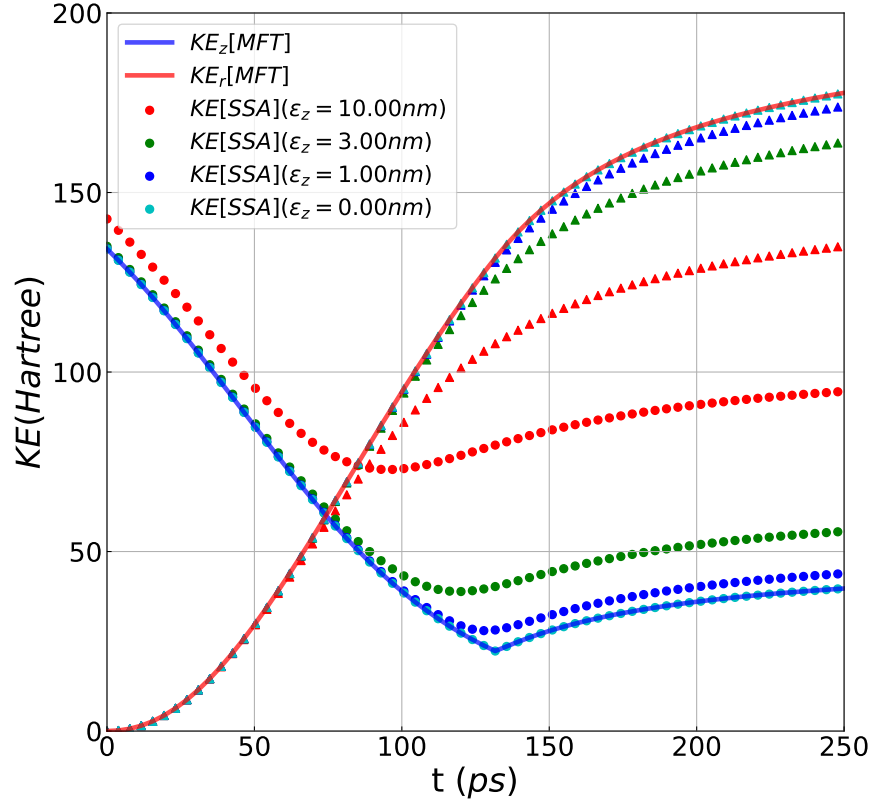
Figure 3.3: Kinetic energy in longitudinal and radial direction for crossover case $(-1.5\omega_c^*$ in $\hat{z}$, corresponding to panel (c) in Fig.3.2), with solid lines for MFT and dotted lines for SSA with different emittance (circle for KE_z and triangle for KE_r). The sudden change of direction for MFT in longitudinal kinetic energy comes from the sign flip of chirp discussed in Sec.2.

of a focusing ellipsoidal electron bunch can be written as:

$$\frac{d}{dt}KE_i = \frac{N}{m}\gamma_i\mathcal{K}_{Fi}(\alpha) \tag{3.57}$$

This evolution is consistent with the fundamental idea that focusing an electron bunch against Coulomb repulsion transfers kinetic energy in the focusing degree of freedom into potential energy while expansion works in the other directions. For example, when the electron bunch is focused in the longitudinal direction, the kinetic energy associated with the longitudinal direction will transfer to the potential energy. Therefore, if one degree of freedom is focusing while the other one is expanding, it would appear to be kinetic energy transfers between two directions. This energy transfer is mediated by the potential energy as the kinetic energy in the focusing direction goes into the potential energy and the potential energy converts to the kinetic energy in the expanding direction. Therefore, we can control this energy transfer process by tuning the focusing procedure.

3.4.3   Statistical discussion and K-V/envelope equations

In this subsection, we want to discuss the statistical essense of the SSA model, namely that the SSA model describes the evolution of second-order moments of the bunch distribution. We compare the force term for both a uniform bunch (Eq. 3.10) and a Gaussian bunch (Eq. 3.55), as the force term for a uniform spheroidal electron bunch can also be evaluated analytically.

Let us take the longitudinal direction of a uniform oblate $(a = b > c)$ spheroidal bunch as an example. For a uniform spheroidal bunch, we can have the following translations between

parameters and bunch statistics:

$$a = \sqrt{5}\sigma_T \tag{3.58a}$$

$$c = \sqrt{5}\sigma_z \tag{3.58b}$$

$$n = \frac{3N}{4\pi a^2 c} \tag{3.58c}$$

The linear coefficient $\mathcal{K}_{Fz}(\alpha)$ in the force terms in the longitudinal direction from Eq. 3.10 can be rewritten as:[7]

$$
\begin{aligned}
\mathcal{K}_{Fz}(\alpha) &= \frac{ne^2}{2\varepsilon_0}a^2 c \int_0^\infty \frac{dl}{(c^2+l)^{3/2}(a^2+l)} \\
&= \frac{1}{4\pi\varepsilon_0}\frac{Ne^2}{c^3}\frac{3}{2}\int_0^\infty \frac{d(l/c^2)}{(1+l/c^2)^{3/2}(a^2/c^2+l/c^2)} \\
&= \frac{1}{4\pi\varepsilon_0}\frac{Ne^2}{5\sqrt{5}\sigma_z^3}\frac{3}{2}\int_0^\infty \frac{d\nu}{(1+\nu)^{3/2}(a^2/c^2+\nu)} \\
&= \frac{1}{4\pi\varepsilon_0}\frac{Ne^2}{5\sqrt{5}\sigma_z^3}\frac{3}{2}\left[\frac{2c^2}{c^2-a^2}\left(\frac{c}{\sqrt{a^2-c^2}}\arcsin\sqrt{1-\frac{c^2}{a^2}}-1\right)\right] \\
&= \frac{1}{4\pi\varepsilon_0}\frac{Ne^2}{5\sqrt{5}\sigma_z^3}L_z\left(\frac{1}{\alpha}\right)
\end{aligned} \tag{3.59}
$$

Similar results apply to the transverse direction and both directions for prolate spheroids as well. We can then rewrite the SSA evolution equations for a uniform spheroidal bunch as:

$$\frac{d\sigma_i^2}{dt} = \frac{2}{m}\gamma_i \tag{3.60a}$$

$$\frac{d\gamma_i}{dt} = \frac{1}{m}\left(\eta_i + \frac{\gamma_i^2}{\sigma_i^2}\right) + \frac{1}{4\pi\epsilon_0}\frac{Ne^2}{5\sqrt{5}}\frac{1}{\sigma_i}L_i\left(\frac{1}{\alpha}\right) \tag{3.60b}$$

$$\frac{d\eta_i}{dt} = -\frac{2\gamma_i\eta_i}{m\sigma_i^2} \tag{3.60c}$$

---

[7]Credits to Brandon Zerbe for the evaluation of the corresponding interals.

with $i = T, z$ for transverse and longitudinal direction, respectively. The impact of the collective Coulomb interaction from a uniform density profile on bunch evolution is strikingly similar to that from a Gaussian bunch (Eq. 3.55). The difference between the two density profiles can be expressed by the ratio of the two force terms as:

$$\frac{K^{Gaussian}}{K^{Uniform}} = \frac{5\sqrt{5}}{6\sqrt{\pi}} \approx 1.0513 \tag{3.61}$$

Therefore, the difference between the two density profiles is only a little over 5%. In other words, according to the SSA model, the evolution of bunch statistics for a uniform bunch with N electrons is identical to that of a Gaussian bunch with the same initial bunch statistics and total number of electrons equals to $0.95N$.

This similarity comes from two key factors: (1) σ_{i,F_i} describes the linear part of the self-field with respect to the corresponding spatial position, which is the only presence of the Coulomb interaction for bunch evolution in the SSA model with the linear chirp assumption (2) the mean-field calculation of the linear part of the self-field (σ_{i,F_i}) shares the similar expression as the second-order moments of spatial coordinates of the bunch distribution [30, 41]. That is the linear approximation of the force distribution depends largely on the second-order moments of the distribution, which is consistent with the argument by Sacherer [34].

The Kapchinsky-Vladimirsky (K-V) envelope equations are well-established in the accelerator community for describing both continuous and bunched beams. It was initially proposed to model beams with uniform density profile and later extended to continuous beams with elliptical symmetry as well as bunched beams with ellipsoidal symmetry. [34] The SSA model is mathematically equivalent to the K-V envelope equations as the SSA uses

similar rms (root-mean-square) bunch statistics for uniform bunch evolution as Sacherer mentioned in his paper. The only difference is that the K-V envelope equation combines the time-derivatives of three bunch statistics in each direction into one ordinary differential equation. The SSA model counterpart related to the varying emittance in K-V envelope equations will be discussed next.

3.4.4   SSA with emittance evolution

The SSA model is capable of estimating the bunch evolution with varying emittance. We can rewrite the SSA model (Eq. 3.6c) as:

$$\frac{d\eta_i}{dt} = \frac{d}{dt}\left(\frac{\varepsilon_i^2}{\sigma_i^2}\right) = -\frac{2\gamma_i\eta_i}{m\sigma_i^2} + \frac{1}{\sigma_i^2}\frac{d\varepsilon_i^2}{dt} \tag{3.62}$$

The first term on the right-hand side (RHS) can be considered as the energy transfer from the linear local average motion to the local momentum fluctuation. The second term on the RHS represents the energy transfer from the potential energy, describing the impact of a varying emittance on local momentum fluctuation. The detailed form of these two terms can be found in Eq. 3.6. Currently, in our research, the emittance evolution can be obtained numerically from simulation data. We discuss our preliminary thoughts about the emittance evolution process in the next chapter. A more thorough study discussing the corresponding analytical models will be presented in future research.

As we present all the models, we test their performance and limitation by comparing them with N-particle simulations, especially the longitudinal focusing of the electron bunches in the next chapter.

Chapter 4

Numerical Simulations

In this chapter, we present the molecular dyamics (MD) simulation results for the evolution of uniform ellipsoidal electron bunches focused by linear longitudinal chirps. We discuss the comparison between the SSA model predictions and the MD simulation results for further understanding of the electron bunch evolution (especially around crossover) and the limitations of the SSA model.

4.1 Simulation method

Although there are many simulation methods that run faster than MD in studying the electron bunch evolution with Coulomb effects, such as the Particle-In-Cell (PIC) method, we rely on the MD simulation due to the fact that it fully preserves the Coulomb interaction information between electrons. Our simulation starts from a uniform ellipsoidal bunch with a non-zero initial emittance, which we refer to as a "warm" initial condition. Then, we solve non-relativistic equations of motion for every electron using the velocity-Verlet integration with the help of the Fast Multipole Method (FMM) from fmmlib3d library [42] calculating the field at the spatial position of each electron.

Here is a simple overview about our MD simulation before we discuss the warm initial conditions and the simulation results. First, we run the simulation in a rest frame to simulate the evolution of an electron bunch in its center of mass frame. Each particle represents one

individual electron. Therefore, each particle/electron j has six attributes in the center of mass frame to describe the phase space position at time t during the simulation: $(\boldsymbol{r}_j = x_j, y_j, z_j)$ for its spatial position in the center of mass frame and $(\boldsymbol{v}_j = v_{xj}, v_{yj}, v_{zj})$ for its relative momentum with respect to the center of mass.

Second, the Coulomb interaction on particle j from all other electrons is calculated by the Fast Multipole Method (FMM), a numerical technique that speeds up the calculation of long-range forces such as Coulomb interaction [42]. It achieves $\mathcal{O}(N)$ time complexity (where N is the total number of particle/electron) by expanding the corresponding Green's function using a multipole expansion, which equivalently groups sources that lie close together and treats them as if they are a single source for long-range interaction.[1]

Third, we use the velocity-Verlet integration scheme as our non-relativistic pusher to propagate the bunch evolution forward in time. Velocity-Verlet integration, similar to the leapfrog integration, is a second-order integration method, that updates positions and velocities at interleaved time points, staggered in such a way that they "leapfrog" over each other. With the force information $\boldsymbol{F}_j(t)$ from the FMM calculation based on the position of particles at time t, the corresponding non-relativistic equation of motion (EOM) for each individual particle (j) is then:

$$\boldsymbol{r}_j(t + \Delta t) = \boldsymbol{r}_j(t) + \left(\boldsymbol{v}_j(t) + \frac{\boldsymbol{F}_j(t)}{m_e} \frac{\Delta t}{2} \right) \Delta t \qquad (4.1a)$$

$$\boldsymbol{v}_j(t + \Delta t) = \boldsymbol{v}_j(t) + \frac{\boldsymbol{F}_j(t) + \boldsymbol{F}_j(t + \Delta t)}{m_e} \frac{\Delta t}{2} \qquad (4.1b)$$

The detailed implementation scheme for this integration is then:

---

[1]An overview of the algorithm and implementation of FMM can be in this lecture notes by Beatson and Greengard [43].

1. propagate the velocity to the middle-point: $\boldsymbol{v}_j(t + \frac{1}{2}\Delta t) = \boldsymbol{v}_j(t) + \frac{\boldsymbol{F}_j(t)}{m_e}\frac{\Delta t}{2}$

2. propagate the position to the next time-point: $\boldsymbol{r}_j(t + \Delta t) = \boldsymbol{r}_j(t) + \boldsymbol{v}_j(t + \frac{\Delta t}{2})\Delta t$

3. Calculate the force $\boldsymbol{F}_j(t + \Delta t)$ based on the new charge distribution $\boldsymbol{r}(t + \Delta t)$

4. propagate the velocity to the next time-point: $\boldsymbol{v}_j(t + \Delta t) = \boldsymbol{v}_j(t + \frac{\Delta t}{2}) + \frac{\boldsymbol{F}_j(t+\Delta t)}{m_e}\frac{\Delta t}{2}$

Essentially, the velocity Verlet takes advantage of staggering the calculation time point for position and velocity to apply mid-point estimation for both the position and the velocity evolution at once.

To assure the validity of the simulation, we check the conservation of energy by calculating the kinetic energy and potential energy of the bunch regularly during the simulation. In this chapter, the representation of the MD simulation data are one line for the mean value of the 90 samples and one same-colored area showing the size of standard deviation across the samples.

The simulations were conducted using in-house code with the field calculation done by the fmmlib3d library. This code has been validated through comparison to another in-house code implementing the brute-force MD code using CUDA.

4.2 Warm initial condition

In this section, we present the "warm" initial condition for the equation of motion (Eq. 4.1) in our MD simulations. In the SSA model and MD simulation, we assume the longitudinal compression process for the probing electron bunch takes place during the free-drifting region between the RF cavity and the specimen. The warm initial condition is a thermalized bunch of particles that represents an electron bunch with a non-zero emittance as our

attempt to mimic the bunch phase-space distribution right after the RF cavity. The warm initial condition helps us to prepare a phase-space distribution of an electron bunch with non-zero emittance.

We first place about 19100 electrons inside a simulation box with periodic boundary condition (PBC) at the target density, which is $10,000$ electrons for a prolate spheroid with the semi-axes of $(10\mu m, 10\mu m, 75\mu m)$. The starting position of each electron is randomly drawn from a uniform distribution and the starting momentum is zero.

Then the electrons interact with each other until the bunch reaches equilibrium. We set the thermalization time to be over 10 plasma oscillation periods because (1) this time period is long enough for bunches to reach equilibrium and (2) the proper travel time from the photo-cathode to the RF cavity is close to the duration of the thermalization process. We refer to this process as the sample thermalization. Since we employ the periodic boundary condition for the sample thermalization, the Particle-Particle-Particle-Mesh (PPPM) method is the preferred standard method as the Particle-Mesh part of PPPM takes advantage of the highly efficient Fast Fourier Transform (FFT) method [44] to speed up the evaluation of the long-range interaction from the PBC. Therefore, the thermalization process of the initial conditions are prepared with the high-performance PPPM feature in LAMMPS [45].

At the end of the thermalization process, we select the electrons which are inside the desired prolate spheroidal region to construct one sample of the warm initial condition. One sample of the warm initial conditions is shown in Fig.4.1. As the initial position is random, the resulting samples will have slight differences in the total number of particles. To mitigate the randomness of starting position, we prepare 90 such samples to obtain reasonable statistical analysis for simulation results. To apply different initial linear chirp into the warm initial conditions, the momentum of each particle is adjusted based on its
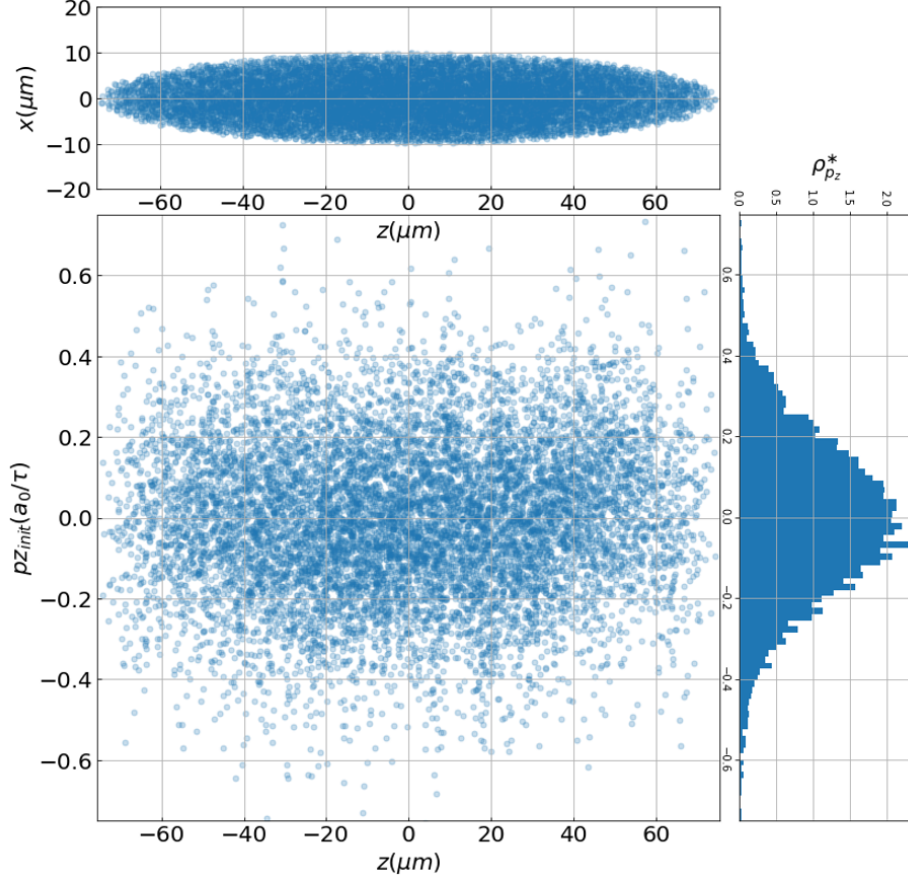
Figure 4.1: The $z - p_z$ phase-space distribution of a warm initial condition. The initial local momentum fluctuation has a Gaussian profile and the corresponding linear chirp is added based on the spatial coordinates of each electron.

spatial coordinates as presented in Eq.3.5.

4.3   Width evolution

In this section, we present the comparison between MD simulation results and the SSA model predictions for the bunch evolution, specifically, the longitudinal focusing process. Several simulations were performed for initial linear chirps: $-0.7\omega_c^*$, $-1.0\omega_c^*$ and $-1.5\omega_c^*$, where ω_c^* is obtained from the MFT calculation in Sec. 2.1.4. As shown in Fig.4.2, the SSA model predictions deviate from the MD simulation results in three familiar aspects:
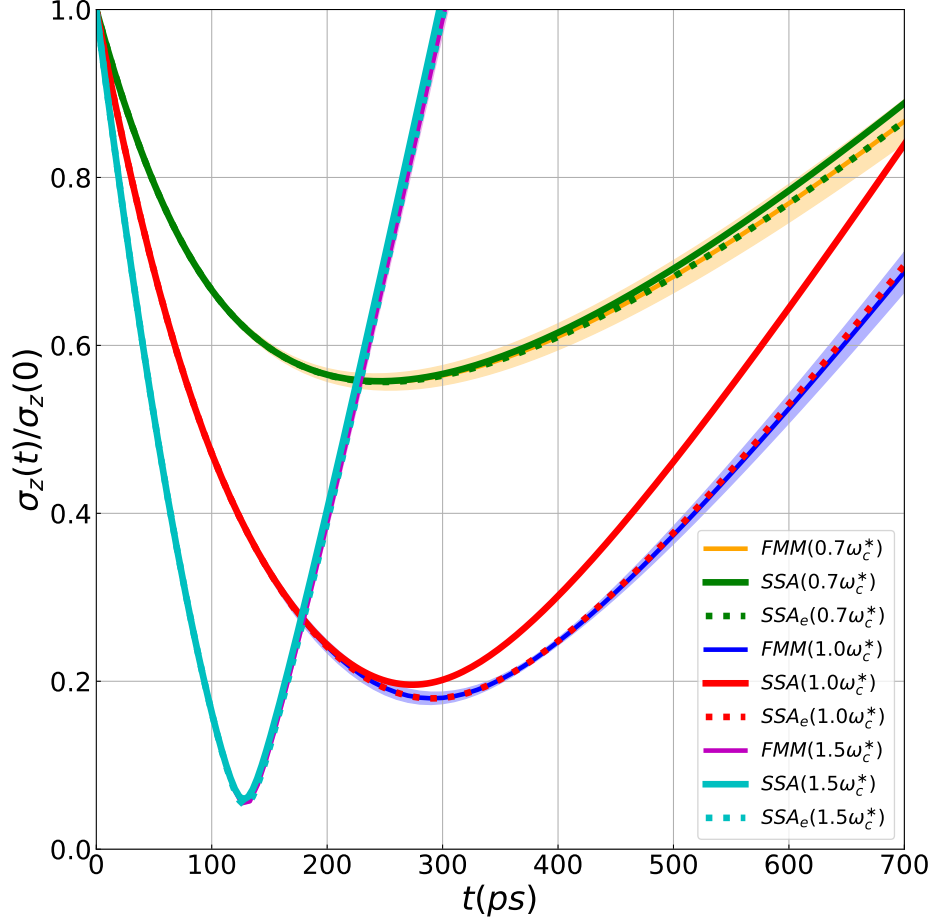
Figure 4.2: Comparison of longitudinal width evolution with different initial chirps from SSA and MD simulations. For each initial chirp, the connected-dots correspond to the average of the 90 MD simulations, the thick solid line is the SSA model prediction with the average emittance of the warm initial conditions. The thick dotted line is the modified SSA considering the emittance evolution in Fig. 4.4. The discrepancy between SSA and MD simulations is driven by the longitudinal emittance decrease, seen in the simulations, which is confirmed by the good agreement between the modified SSA and simulations.

(1) a slightly larger minimum width, (2) the critical time to reach the minimum width is smaller and (3) the discrepancy between SSA and MD is most significant when the bunch is compressed at the critical chirp, where the bunch evolution is most sensitive to different emittance as we discussed in the last section. We previously saw similar trends in the minimum width and the time to reach the minimum width as we discussed in Fig. 3.2. As the input for the SSA model prediction in Fig. 4.2 already includes the mean value of

the initial emittance across the 90 simulation samples, this suggests that the longitudinal emittance may be decreasing during the MD simulations. The rms emittance evoluiton in panel (b) of Fig.4.4 confirms the decrease of longitudinal emittance, with several interesting features we are going to discuss later.

As discussed previously, the mathematical mechanism behind the conservation of emittance in the SSA is the vanishing of the following term associated with emittance evolution in Eq. 3.6:

$$\sigma_i^2 \sigma_{p_i, F_i} - \sigma_{i, p_i} \sigma_{i, F_i} = 0$$

Currently we are working on the analytical theory to predict the evolution of these terms in either a continuum approximation of the SSA model or the discrete particle settings like the MD simulations.

However, we can extract the evolution of emittance from the simulation data to better capture the accuracy of the model predictions. Specifically, as we discussed in Sec. 3.4.4, we replace Eq. 3.6c by Eq. 3.62:

$$\frac{d\eta_i}{dt} = \frac{d}{dt}\left(\frac{\varepsilon_i^2}{\sigma_i^2}\right) = -\frac{2\gamma_i \eta_i}{m\sigma_i^2} + \frac{1}{\sigma_i^2}\frac{d\varepsilon_i^2}{dt}$$

in the SSA model with the time derivative of emittance square ($d\varepsilon_i^2/dt$). The first term on the right-hand side (RHS) can be considered as the communication between the linear local average momentum and the local momentum fluctuation. This term comes from the non-interacting kinematics as expansion reduces η_i and compression increases η_i. The second term represents the energy transfer between the potential energy to η_i, which can be obtained from the simulation data.

The evolution of the longitudinal width and the kinetic energy associated with the elec-

tron motion in the longtudinal direction using this modification can be seen as the dotted

lines in Fig.4.2 and Fig. 4.3, respectively. Excellent agreement between these modified SSA
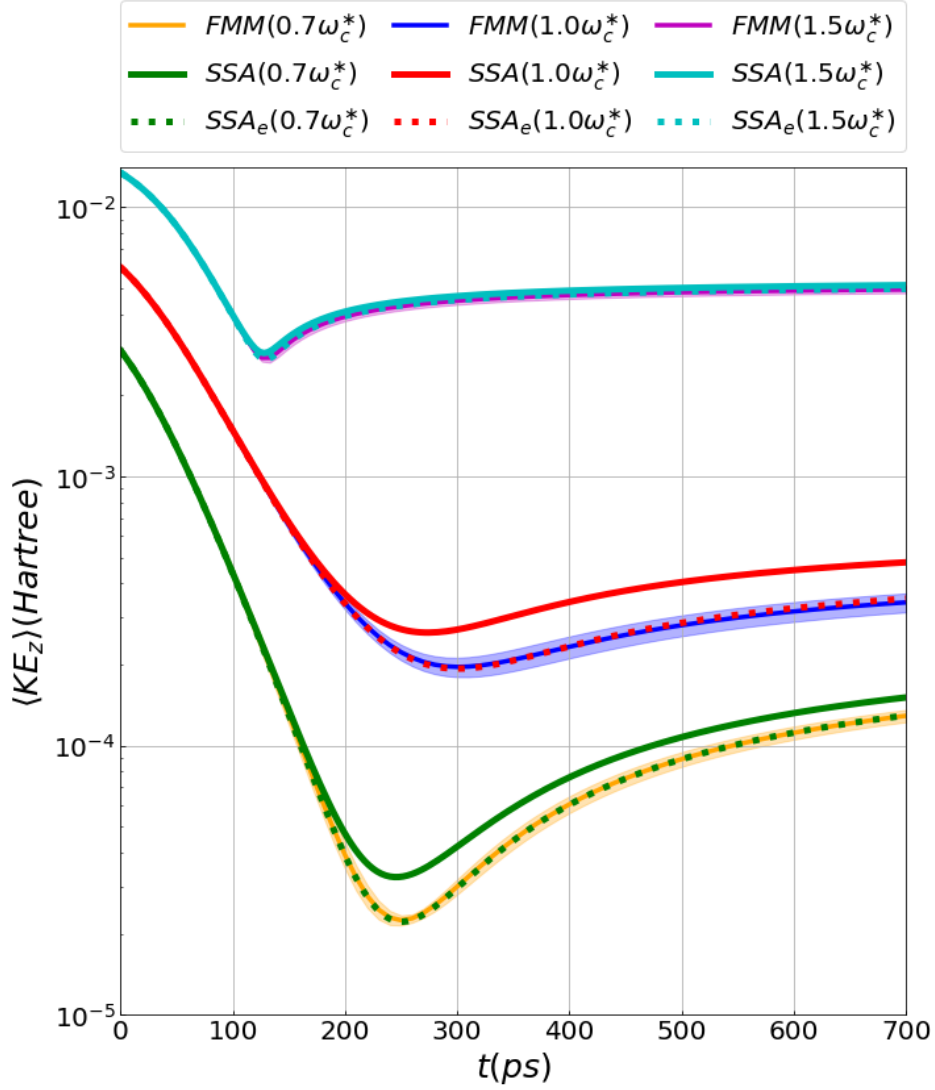
Figure 4.3: Comparison of kinetic energy associated with the longitudinal motion of the electrons relative to the bunch center of mass with different initial chirps from SSA and MD simulations. For each initial chirp, we have the connected-dots are the corresponding 90 MD simulations, the thick solid line for SSA prediction with the average emittance of those warm initial conditions and the thick dotted line for the modified SSA considering the emittance evolution in Fig.4.4.

model predictions and the MD simulation results suggests that varying emittance is the main

factor causing the discrepancy between the longitudinal spatial variance and longitudinal

kinetic energy evolution of the (constant-emittance) SSA model and the MD simulations. Therefore, if the evolution of the covariance term σ_{p_i, F_i} and σ_{i, F_i} can be understood and modeled, we should be able to obtain the SSA model that captures the expected behavior of electron bunches to a high degree of accuracy.

4.4   Emittance evolution

In this section, we discuss our preliminary thoughts about the emittance evolution process, specifically discussing the electron bunch focusing process, while more thorough studies and corresponding analytical models will be presented in the future.

For now, the emittance evolution can be obtained numerically from the simulation data as shown in Fig. 4.4. The emittance evolution in Fig. 4.4, especially simultaneous increase for both the longitudinal and transverse emittance, cannot be explained by the popular heat transfer mechanism employed in the literature [46]. On one hand, as can be seen in panel(b) of Fig. 4.4, the longitudinal emittance increases slightly at the beginning of the simmulation followed by a gradual decrease. In addition, there is another rapid increase in the longitudinal emittance close to t_c for the simulations in the crossover regime. On the other hand, in panel (a) of Fig.4.4, the transverse emittance likewise has a slight increase at the beginning of the simulation followed by a gradual increase. Notice that again for the simulations in the crossover regime, there is a rapid increase around t_c as well. We would like to emphasize that the rapid increase in the emittance of both directions are almost coincidental — an observation that is not predicted in the literature and cannot be explained by the heat transfer mechanism.

We propose two mechanisms, Disorder-Induced Heating (DIH) and emittance transfer,
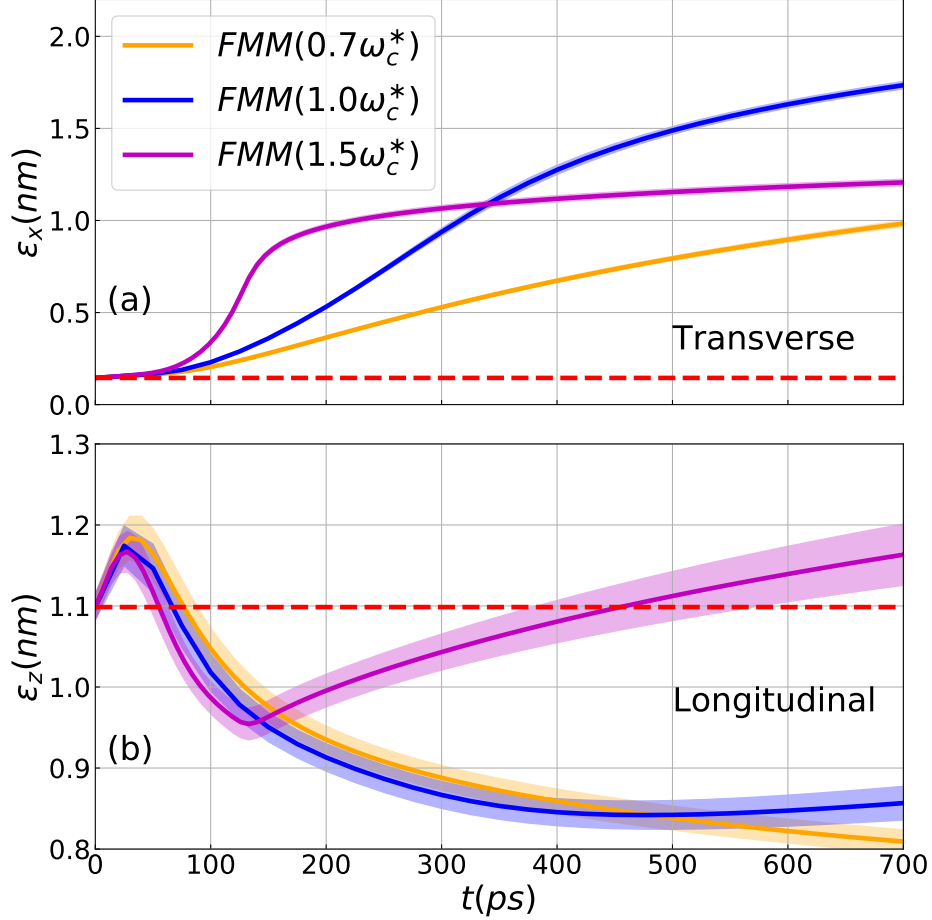
Figure 4.4: (rms) Emittance evolution in (a) transverse ε_x and (b) longitudinal ε_z direction for three different initial chirps.

for driving the emittance evolution in the MD simulations [35] as discussed in the following two subsections.

4.4.1 Disorder-induced heating (DIH)

DIH in the plasma community describes the heating process during the transition of a bunch from a disordered state to an ordered state which is structured by Coulomb forces [47–51]. We argue that there are two phases during the MD simulations where significant emittance growth is generated by this mechanism: (1) the sudden removal of the thermalization confinement at the beginning of the simulation and (2) around the critical time t_c,

especially for the simulations in the crossover regime.

First, we attribute the emittance increase at the beginning of the simulation to DIH. With the sudden removal of surrounding electrons and the periodic boundary condition, the already thermalized electron bunch is suddenly not at equilibrium in the new circumstance. The bunch can be considered as a disordered state and it starts to evolve towards its new equilibrium with the influence of Coulomb interaction. The heat transfer from potential energy to the local momentum fluctuation during this initial phase of the simulation can then be explained by DIH.

The second situation for DIH induced emittance growth happens around the critical time (t_c) or focal point where a bunch reaches its minimum. In Fig. 4.5, we present the bunch density distribution in MD simulations throughout the crossover evolution, and its comparison with the density profile of a uniform ellipsoid with the same longitudinal spread. Since the difference is most significant at t_c, DIH suggests a significant amount of heat is injected into the kinetic energy associated with the local momentum fluctuations. In other words, the focusing process of the uniform bunch (especially for the cases in crossover regime) pushes the bunch further away from its equilibrium state, resulting in a highly non-equilibrium state at t_c. The relaxation of this highly non-equilibrium state is another demonstration of disorder induced heating. As such DIH coming from the potential energy is isotropic, we see a sudden increase in the emittance in both the longitudinal and transverse direction almost simultaneously. A detailed discussion about this DIH and its possible connection to the Boersch effect can be found in the following sections. Moreover, Eq. 3.62 also indicates this emittance increase is further amplified at crossover where σ_z^2 reaches its minimum. Therefore, a significant longitudinal emittance boost is observed around t_c in the crossover case in panel (b) of Fig.4.4.
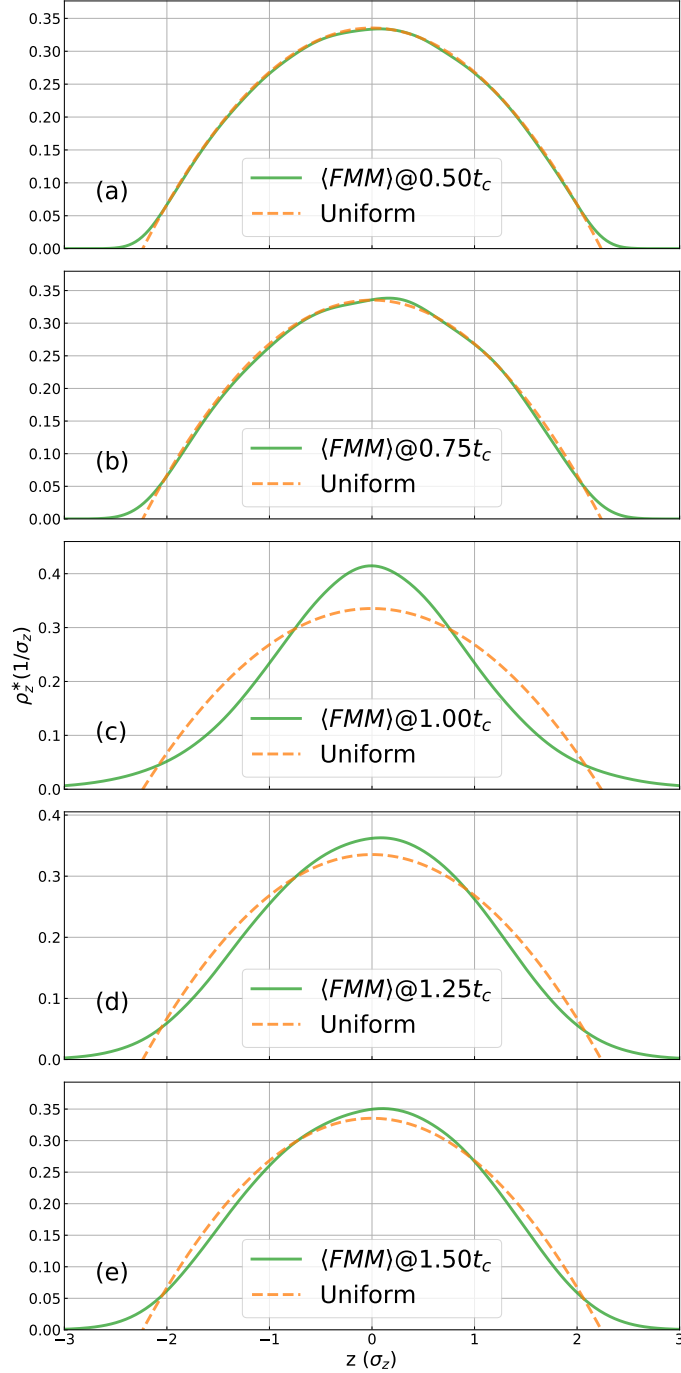
Figure 4.5: Longitudinal density profile evolution of crossover case $(-1.5\omega_c^*)$ with the longitudinal width scaled by its standard deviation. In each panel, solid line represents the average of simulation samples and dotted line is the density profile for a uniform spheroid of the same longitudinal width with simulation data. The deviation from uniformity is most prominent at crossover. Note however, tails of the distribution present in simulations at all initial chirps.

4.4.2 Emittance transfer between degrees of freedom

In our MD simulations for the longitudinal focusing of the electron bunch, the longitudinal emittance decreases due to the heat transfer to the transverse direction. Here the expression $\frac{1}{2m_e}\eta_i$ is considered to be the SSA temperature of each degree of freedom because (1) $\frac{1}{2m_e}\eta_i$ can be considered as the kinetic energy or temperature associated with the local momentum fluctuation, and since η_i is the variance of the local momentum fluctuations with respect to the linear local average momentum.

Figure 4.6: The variance of the local momentum fluctuations for the case in bounce-back regime ($0.7\omega_c$) on a Log-Log scale.

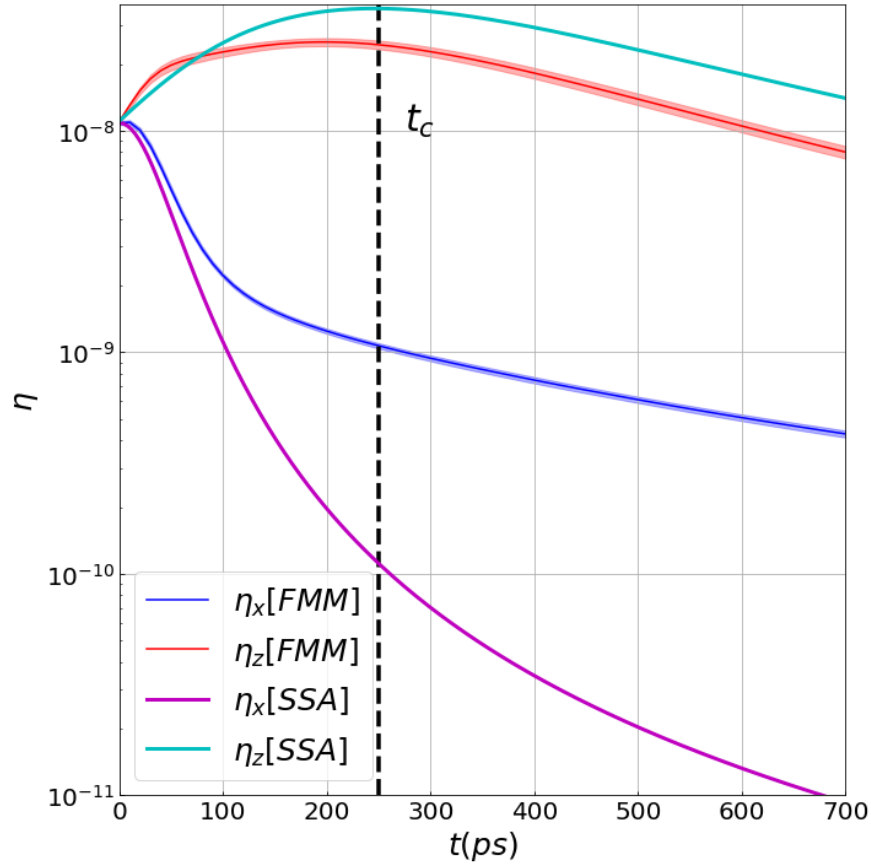Although the equilibrium requirement for a strict definition of temperature is not appropriate for the highly non-equilibrium electron bunches in this analysis, we want to borrow

the temperature concept to facilitate our discussion about the heat/emittance transfer. At the begining of the simulation, the initial value of the SSA temperature in both longitudinal and transverse directions are similar to each other. Eq. 3.6c and Eq. 3.62 suggest that the longitudinal SSA temperature (η_z) increases as the electron bunch focuses in the longitudinal direction, while the transverse SSA temperature decreases due to the expanding transverse direction. Therefore, this SSA temperature difference between the two direction increases as the bunch evolves towards the focal point. We would expect a heat transfer from the hotter longitudinal direction to the cooler transverse direction in such circumstances. This heat transfer is achieved through the exchange between potential energy and the variance of local momentum fluctuation η_i of each direction. The immediate result of this heat transfer can be seen in Fig. 4.6 where η_z from the MD simulations is smaller than that from the SSA model while η_x in the simulation is larger than the model prediction.

This heat transfer is further illustrated in Fig.4.7 as we plot the term associated with the impact of a non-conserved emittance in Eq.3.62 for the dynamics of η_i. After the initial DIH effect at the beginning, the increasing SSA temperature difference generates stronger heat transfer from longitudinal direction to transverse direction. Prior to t_c, the consistent and accelerating heat transfer from the longitudinal direction into the transverse direction is evidence of the emittance transfer between the two degrees of freedom.

Around t_c, a heat influx from the potential energy is observed in both the longitudinal and transverse directions as the electron bunch relaxes from the highly non-equilibrium state around t_c. Notice that the heat influx for the bounce-back cases are smaller than the cross-over cases, and the non-equilibrium effect is more drastic for the cross-over cases as the density profiles are further away from unifrom than the bounce-back case. The discussion about the density profile at t_c can be found in next section. Furthermore, the
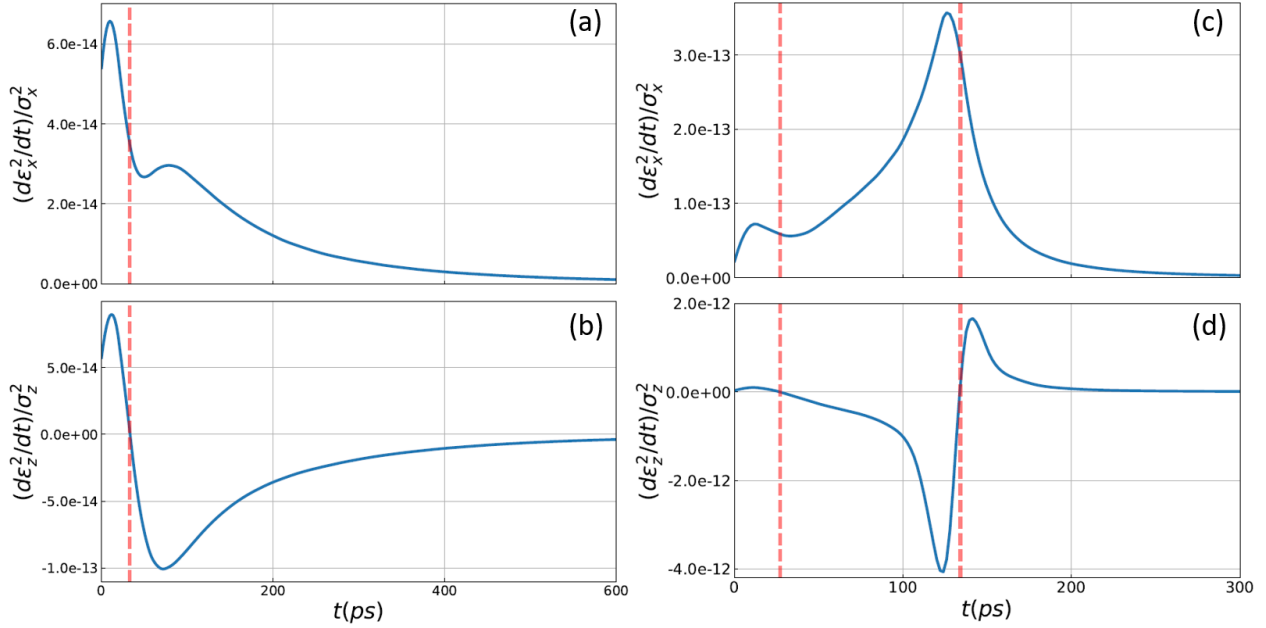
Figure 4.7: The heat transfer from potential to η_i (a) and (b) for bounce-back case $(0.7\omega_c)$; (c) and (d) for cross-over case $(1.5\omega_c)$. The red dotted lines are the time when the transfer in longitudinal direction switches sign.

non-equilibrium state at t_c for cross-over case is so drastic that the heat continues to transfer from the potential energy to the local momentum fluctuation well beyond t_c, as can be seen in panel (c) and (d) in Fig. 4.7.

4.4.3 Phenomenological description of the emittance evolution

Due to the similarity in the longitudinal width evolution of the MD simulation results and the (constant-emittance) SSA predictions in Fig.4.2, the emittance evolution is largely driven by the change in η_i.

The two competing mechanisms result in the following three phases for the emittance evolution for bunches that are compressed longitudinally: (1) Initial phase dominated by DIH: at the beginning of simulation, the DIH due to the removal of the thermalization confinement is the driving factor that increases the emittance in both longitudinal and transverse

direction; (2) Emittance transfer phase: the SSA temperature difference increases as the bunch evolves, the emittance transfer mechanism overwhelms the initial DIH, resulting in the decrease in longitudinal emittance and increase in transverse emittance; (3) DIH around t_c: for the cases in the cross-over regime, the bunch reaches a highly non-equilibrium state when it approaches its minimum width around t_c, creating another circumstance for a significant DIH effect. The relaxation of this DIH leads to the sudden emittance growth in both the longitudinal and transverse direction in Fig.4.4.

4.5   Density profile at t_c

In this seciton, we further study the highly non-equilibrium state and the corresponding DIH effect around t_c. We present the spatial density profile of one MD simulation sample in the cross-over regime and the corresponding SSA estimation and uniform density profile in Fig. 4.8.

We generate the histogram and the corresponding kernel density estimation (KDE) from the z coordinates of the electrons in the bunch at t_c. By comparing the simulation result with the uniform density profile of the same longitudinal variance, it is clear that the density profile in the longitudinal direction of the MD simulation at t_c deviates significantly from the uniform profile.

4.5.1   Density profile prediction from SSA and its linear chirp assumption

We discuss the density profile at t_c determined from the SSA model prediction, followed by a discussion of its linear-chirp assumption.
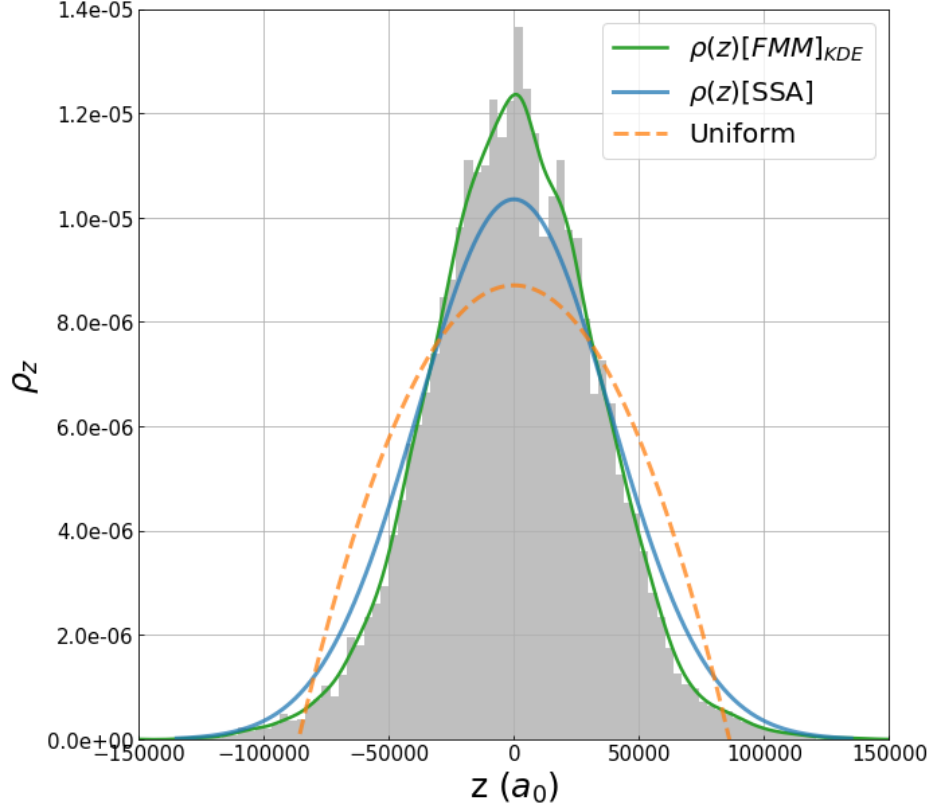
Figure 4.8: Longitudinal density profile at t_c of one crossover case $(-1.5\omega_c^*)$. The grey histogram represents the electron distribution along the longitudinal direction of the simulation sample at t_c. The green solid line is the corresponding kernel density estimation (KDE) of the density distribution. The blue solid line is the corresponding density profile from the SSA calculation of that sample. The orange dotted line is representing the density distribution of a uniform spheroid with the same longitudinal spread.

The density profile at any given time $t > 0$ can be obtained by progressing the phase-space distribution from the known initial distribution of $(\tilde{z}, \tilde{p_z})$ before adding the chirp to $(z(0), p_z(0))$:

$$dQ = S(\tilde{z})d\tilde{z}G(\tilde{p_z})d\tilde{p_z} \qquad (4.2)$$

with $S(\tilde{z})$ representing a uniform distribution with the spheroidal shape and $G(\tilde{p_z})$ representing an independent Gaussian profile of initial momentum spread without a chirp, as

shown in Fig. 4.1:

$$S(\tilde{z}) = \pi a^2 \left[1 - \left(\frac{\tilde{z}}{c} \right)^2 \right] \tag{4.3a}$$

$$G(\tilde{p}_z) = \exp\left[-\frac{\tilde{p}_z^2}{2\eta} \right] \tag{4.3b}$$

from the initial bunch size $(a(0), c(0))$. Adding the linear chirp γ/σ^2 simply means one extra transformation:

$$\begin{bmatrix} z(0) \\ p_z(0) \end{bmatrix} = \begin{bmatrix} 1 & 0 \\ \gamma/\sigma^2 & 1 \end{bmatrix} \cdot \begin{bmatrix} z_0 \\ p_{z0} \end{bmatrix} \tag{4.4}$$

The transfer matrix $T(t)$ for the trajectory of every particle according to the linear force in SSA is then:

$$\begin{bmatrix} z(t) \\ p_z(t) \end{bmatrix} = \lim_{\Delta t \to 0} \prod_{i=0}^{t/\Delta t} \begin{bmatrix} 1 & \frac{1}{m_e}\Delta t \\ \mathcal{K}_{Fz}[\alpha(i\Delta t)] \cdot \Delta t & 1 \end{bmatrix} \cdot \begin{bmatrix} z(0) \\ p_z(0) \end{bmatrix} = T(t) \cdot \begin{bmatrix} z(0) \\ p_z(0) \end{bmatrix} \tag{4.5}$$

where $T(t)$ and its inverse $T^{-1}(t)$ can then be obtained through numerical solutions for the dynamics of the SSA model:

$$\begin{bmatrix} z(0) \\ p_z(0) \end{bmatrix} = T^{-1}(t) \cdot \begin{bmatrix} z(t) \\ p_z(t) \end{bmatrix} = \begin{bmatrix} T_{11}^{-1}z(t) + T_{12}^{-1}p_z(t) \\ T_{21}^{-1}z(t) + T_{22}^{-1}p_z(t) \end{bmatrix} \tag{4.6}$$

and

$$\begin{bmatrix} \tilde{z} \\ \tilde{p}_z \end{bmatrix} = \begin{bmatrix} 1 & 0 \\ -\gamma/\sigma^2 & 1 \end{bmatrix} \cdot \begin{bmatrix} z(0) \\ p_z(0) \end{bmatrix} = \begin{bmatrix} 1 & 0 \\ -\gamma/\sigma^2 & 1 \end{bmatrix} \cdot T^{-1}(t) \cdot \begin{bmatrix} z(t) \\ p_z(t) \end{bmatrix} \tag{4.7}$$

So then the longitudinal density distribution function of the SSA model reads:

$$\rho(z;t)dz = \int S(\tilde{z}_{z(t),p_z(t)})d\tilde{z}G(\tilde{z}_{z(t),p_z(t)}, \tilde{p}_{z\,z(t),p_z(t)})d\tilde{p}_z$$

$$= dz \int \pi a^2 \left[1 - \left(\frac{\tilde{z}_{z(t),p_z(t)}}{c}\right)^2\right] \exp\left[-\frac{\left(\tilde{p}_{z\,z(t),p_z(t)}\right)^2}{2\eta_z}\right] dp_z \qquad (4.8)$$

with the help of the Liouville's theorem, i.e. $d\tilde{z}d\tilde{p}_z = dz(t)dp_z(t)$. Therefore, we obtain the projected density profile according to the SSA model as the blue solid line in Fig.4.8, which also deviates quite significantly from a uniform density profile as the SSA model assumed.

This derivation has a caveat that the transformation leads to a bell-shaped density profile while the driving T matrix is calculated following the uniform density profile assumption in the SSA model. In other words, we model the bunch evolution using a uniform density profile while the actual density distribution is not strictly uniform. However, from the accuracy prospective, if the deviation from the uniform density profile is not too significant (for bounce-back case) and not lasting too long (for cross-over case), the predictions of SSA are still in a good agreement with the simulation results as we can see from Fig. 4.2. The cases driven by the critical chirp present the most significant discrepancy between the simulation and the model.

This deviation from uniform density profile illustrated both the limitation and versatility of the SSA model. The limitation lies as it relies on the linear chirp assumption to conserve emittance while only the uniform bunch with zero emittance can maintain that linear chirp assumption throughout the bunch evolution. The versatility of SSA is that with the addition of the emittance change term, the modified SSA model is a complete statistical model that focuses on the evolution of bunch statistics.

4.6 Bunch phase space display for cylindrical bunch

The MD simulation provides the detailed phase-space structure for the bunch evolution. It can be particularly helpful for the bunch profiles that are hard to model. For example, the initial bunch shape might be closer to a cylinder after passing through an aperture, which is helpful in reducing the emittance by removing the hot region on the out-skirts of the bunch [17]. For modeling the focusing process of such bunches, we simulate a uniform bunch starting with cylinder shape with a linear chirp in the longitudinal direction. Fig. 4.9 shows
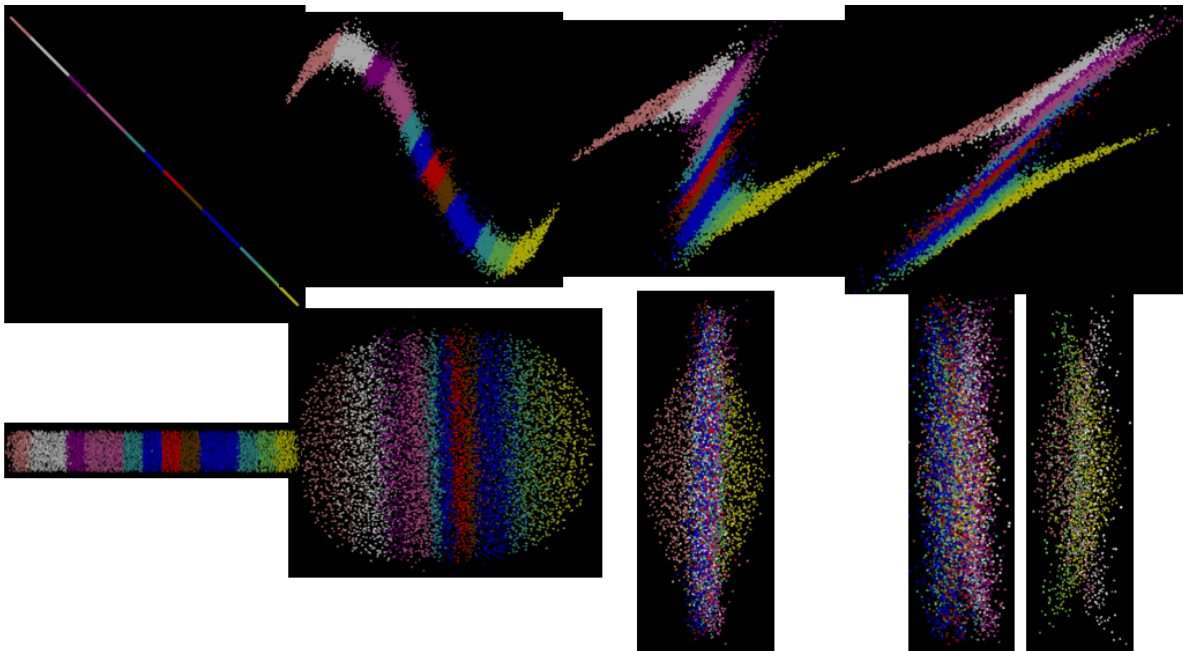
Figure 4.9: The longitudinal phase-space (first row) and real-space (second row) distribution evolution of a uniform bunch, which starts with a cylindrical shape, zero emittance and a linear longitudinal chirp. Electrons are colored based on their initial longitudinal position.

an interesting non-linear phase-space and real-space electron distribution. Specifically, by comparing the phase-space and real-space distribution, we realized that the non-linearity in the phase-space distribution (the hook on the both ends) comes from the center of the front and back end in the longitudinal direction, as the net effect of Coulomb repulsion from the "extra" electrons that are initially outside of the ellipsoidal region is most significant in those

two regions. Furthermore, the Coulomb repulsion from those extra electrons prevents the electrons in those two regions from crossing the bunch center, resulting in a partial-crossover situation.

4.7   Discussion

In this chapter, we present the MD simulation results for the longitudinal focusing process of uniform spheroidal electron bunches. We equilibrate the electrons for the warm initial condition to minimize the initial emittance growth due to DIH. The comparison of the longitudinal width evolution between the MD simulations and the SSA predictions shows the impact of a varying emittance on bunch evolution. We propose two competing mechanisms for the change of emittance throughout the compression process. The DIH increases the emittance in both degrees of freedom while the difference in the SSA temperature generates emittance transfer bewteen degrees of freedom. In addition, the non-uniform density profile at the focal point (t_c) introduces significant DIH that increases the emittance in both longitudinal and transverse directions. The MD simulations also unveil other interesting phase-space structures during the bunch focusing process.

In this section, we extend our discussion about the MD simulation results and the comparison between the MD simulation and the SSA model.

4.7.1   More on the emittance evolution

In Sec. 4.4.2, we discussed the heat transfer due to the SSA temperature difference in the longitudinal and transverse directions. In addition to the bounce-back example in Fig.4.6, we present the evolution of η_i for a crossover case, with the comparison to the SSA model

prediciton in Fig. 4.10. The heat influx in the transverse direction is much more significant
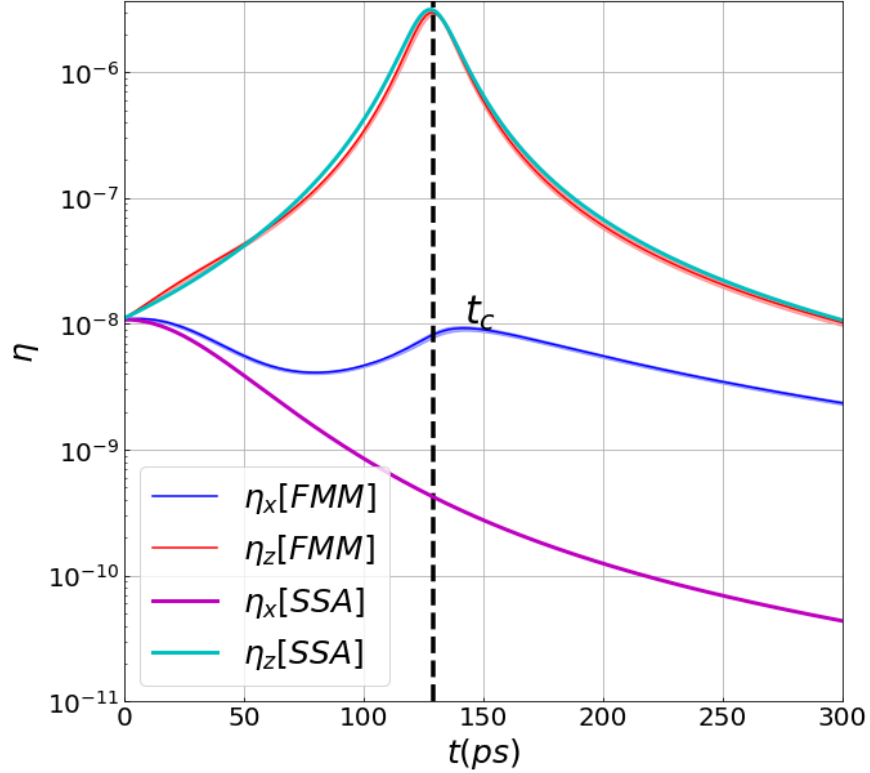
Figure 4.10: The variance of the local momentum fluctuations for the cases in the cross-over regime $(1.5\omega_c)$ on a Log-Log scale.

than that in the bounce-back case. As the bunch evolves far beyond t_c, we would expect η_z and η_x to become closer due to the emittance transfer. However, that is not obvious from Fig.4.6 and Fig. 4.10. The possible explanation could be that the exchange between η_i and the linear average motion within each direction, $-\frac{2\gamma_i\eta_i}{m_e\sigma_i^2}$, can be significantly larger than the heat transfer between directions, as the γ_i increases along with the evolution.

While the two mechanisms for emittance dynamics, DIH and emittance transfer, is qualitatively reasonable, it would be more convincing if we can provide more quantitative estimation to differentiate the effect of these two mechanisms. Specifically, our future work will focus on analytical models to quantify the DIH for the relaxation process from the bell-shaped density profile to a uniform distribution as shown in Fig. 4.5. Nonetheless,

using these two mechanisms, we reach a phenomenological description about the emittance evolution during the longitudinal focusing process of uniform ellipsoidal bunches.

4.7.2 Boersch effect

In addition to the emittance growth, the DIH around t_c also leads to the broadening of the energy spread for the probing electron bunches, which is often referred as the energetic Boersch effect [18, 52–54].

Originally, the Boersch effect was describing the broadening of the energy spectrum in relativistic continuous beam, especially after the beam was focused transversely. One of the explanations in accelerator community attributes the Boersch effect to the heat exchange between the transverse and longitudinal directions through the stochastic collisions between electrons [46, 54–60].

This explanation may not applicable to the similar broadening for the bunched beams like the probing electron bunches in UEM. In the MD simulations for the longitudinal focusing process of the probing electron bunch, the dramatic increase of emittance (and local momentum fluctuation) occurs almost simultaneously in both directions, which cannot be explained by the heat transfer between different degrees of freedom. In addition, there is the difference between the cylindrical symmetry of continuous beams and the ellipsoidal symmetry of bunched beams. Specifically, the focusing process that triggers the Boersch effect is different for continuous beams and bunched beams. For example, the transverse focusing of the bunched beams leads to the entire bunch being compressed in the transverse direction and expanding in the longitudinal direction. However, for the continuous beams, only the waist section being compressed into a smaller transverse cross-section, while the corresponding expansion in the longitudinal direction is omitted due to the cylindrical

symmetry.

One caveat of this analysis is that the MD simulations are done using a non-relativistic pusher in the center of mass frame, while the probing bunches are traveling with a velocity of $0.55c$ in the UEM experiments [18]. Nonetheless, more efforts are required to fully understand the Boersch effect of the bunched beams such as the probing electron bunch in ultrafast experiments.

4.7.3   Sampling error

As we presented in Fig.4.4, the emittance of a uniform bunch evolves quite dramatically in our MD simulations. Another perspective of understanding the origin of emittance evolution might be the sampling error. Specifically, the SSA model (and all other analytical models) treats the electron bunch as a continuum object, while the electron bunch in MD simulations consists of discrete electrons randomly drawn from the uniform distribution. Thus, the SSA model can be considered as a statistical description for the population and each simulation is just one finite-sized sample drawn from the population. In this sense, the simulation introduces sampling errors so that the measurement of the sample deviates from the true value of the population. For example, we assume that some bunch statistics like $\langle z \rangle$, σ_{z,δ_z} are zero in the model, which are most likely non-zero in the simulations.

It is unclear if there is a recovery mechanism for this sampling error. The recovery mechanism here is designated to the intrinsic feature of the statistics or kinematics or Coulomb interaction that reduces the deviation between the sample and the population towards zero as the sample/bunch evolves. From the model and existing simulation results, there is no such effect or the magnitude is not significant enough, i.e. the deviation between a single simulation and the SSA model does not decrease from the initial sampling error. Further

analytical study, such as the impact due to different size of sampling error, is needed to help us understand the origin of this emittance change mechanism.

APPENDIX

Appendix

Detailed derivation for electrostatic potential for uniform ellipsoid

In this appendix, we present the detailed derivation for Coulomb potential for uniformly charged ellipsoids. The derivation is generally folllowed MacMillan's book [36].

The surface of a given uniform ellipsoid with semi-axes (a, b, c) is defined by equation:

$$\frac{\xi^2}{a^2} + \frac{\eta^2}{b^2} + \frac{\zeta^2}{c^2} = 1 \tag{.1}$$

Let the interior point for which the potential is to be computed be $P(x, y, z)$. On taking P as the origin of a spherical coordinates system ρ, φ, θ with the transformation:

$$\xi = x + \rho \cos \varphi \cos \theta \tag{.2a}$$

$$\eta = y + \rho \cos \varphi \sin \theta \tag{.2b}$$

$$\zeta = z + \rho \sin \varphi \tag{.2c}$$

and the corresponding charge element

$$dq = \rho_c \rho^2 \cos \varphi d\varphi d\theta d\rho \tag{.3}$$

with the volume charge density $\rho_c = n \cdot e$ (typically n is the electron number density). Then, the electrostatic potential at point P (with respect to the potential zero point at infinity) is expressed as:

$$V(x, y, z) = \frac{\rho_c}{4\pi\varepsilon_0} \int_E \frac{dq}{\rho} = \kappa \int_{-\frac{\pi}{2}}^{+\frac{\pi}{2}} \int_0^{2\pi} \int_0^{\rho_1(\theta,\varphi)} \rho \cos \varphi \, d\varphi \, d\theta \, d\rho \tag{.4}$$

We substitute $\kappa = \frac{\rho_c}{4\pi\varepsilon_0}$ to simplify the derivation.

The upper limit $\rho_1(\theta, \varphi)$ of the integration with respect to ρ is a function of θ and φ, since the integration is from P to a point on the surface of the ellipsoid. So, we can insert Eq. .2a into Eq. .1 for ρ_1 as:

$$A\rho_1^2 + 2B\rho_1 + C = 0 \tag{.5}$$

where

$$A = \frac{\cos^2 \varphi \cos^2 \theta}{a^2} + \frac{\cos^2 \varphi \sin^2 \theta}{b^2} + \frac{\sin^2 \varphi}{c^2} \tag{.6a}$$

$$B = \frac{x \cos \varphi \cos \theta}{a^2} + \frac{y \cos \varphi \sin \theta}{b^2} + \frac{z \sin \varphi}{c^2} \tag{.6b}$$

$$C = \frac{x^2}{a^2} + \frac{y^2}{b^2} + \frac{z^2}{c^2} - 1 \tag{.6c}$$

With A being positive and C being negative for interior points, ρ_1 is then the positive root of Eq. .5 as:

$$\rho_1 = \frac{-B + \sqrt{B^2 - AC}}{A} \tag{.7}$$

To compute V, we can take the advantage of $\int_0^{\rho_1} \rho \, d\rho = \frac{1}{2}\rho_1^2$, so that Eq..4 becomes

$$V = \frac{\kappa}{2} \int_{-\frac{\pi}{2}}^{+\frac{\pi}{2}} \int_0^{2\pi} \frac{2B^2 - AC - 2B\sqrt{B^2 - AC}}{A^2} \cos \varphi \, d\varphi \, d\theta \tag{.8}$$

90

The second part of the integral vanishes as

$$R = \kappa \int_{-\frac{\pi}{2}}^{+\frac{\pi}{2}} \int_{0}^{2\pi} \frac{B\sqrt{B^2 - AC}}{A^2} \cos\varphi d\varphi d\theta = 0 \tag{.9}$$

can be evaluated by taken in pairs the two elements canceling out each other, e.g. (θ_0, φ_0) and $(\theta_0 + \pi, -\varphi_0)$. The integral reduces to

$$V = \frac{\kappa}{2} \int_{-\frac{\pi}{2}}^{+\frac{\pi}{2}} \int_{0}^{2\pi} \frac{2B^2 - AC}{A^2} \cos\varphi d\varphi d\theta \tag{.10}$$

Substituting the B value from Eq. .6 and we get

$$V = \kappa \Big[\int_{-\frac{\pi}{2}}^{+\frac{\pi}{2}} \int_{0}^{2\pi} \left\{ \frac{\cos^2\varphi \cos^2\theta}{a^2} \cdot \frac{x^2}{a^2} + \frac{\cos^2\varphi \sin^2\theta}{b^2} \cdot \frac{y^2}{b^2} + \frac{\sin^2\varphi}{c^2} \cdot \frac{z^2}{c^2} \right\} \frac{\cos\varphi d\varphi d\theta}{A^2}$$

$$+ 2 \int_{-\frac{\pi}{2}}^{+\frac{\pi}{2}} \int_{0}^{2\pi} \left\{ \frac{xy \cos^2\varphi \cos\theta \sin\theta}{a^2 b^2} + \frac{yz \cos\varphi \sin\varphi \sin\theta}{b^2 c^2} + \frac{zx \cos\varphi \sin\varphi \cos\theta}{c^2 a^2} \right\} \frac{\cos\varphi d\varphi d\theta}{A^2}$$

$$- \frac{C}{2} \int_{-\frac{\pi}{2}}^{+\frac{\pi}{2}} \int_{0}^{2\pi} \frac{\cos\varphi d\varphi d\theta}{A} \Big]$$

$$\tag{.11}$$

By properly pairing the elements in the second integral vanishes, as

$$xy \int_{-\frac{\pi}{2}}^{+\frac{\pi}{2}} \int_{0}^{2\pi} \frac{\cos^2\varphi \cos\theta \sin\theta}{a^2 b^2} \cdot \frac{\cos\varphi d\varphi d\theta}{A^2} \qquad with \quad \{(\theta_0, \varphi_0), (2\pi - \theta_0, \varphi_0)\}$$

$$yz \int_{-\frac{\pi}{2}}^{+\frac{\pi}{2}} \int_{0}^{2\pi} \frac{\cos\varphi \sin\varphi \sin\theta}{b^2 c^2} \cdot \frac{\cos\varphi d\varphi d\theta}{A^2} \qquad with \quad \{(\theta_0, \varphi_0), (2\pi - \theta_0, \varphi_0)\}$$

$$zx \int_{-\frac{\pi}{2}}^{+\frac{\pi}{2}} \int_{0}^{2\pi} \frac{\cos\varphi \sin\varphi \cos\theta}{a^2 b^2} \cdot \frac{\cos\varphi d\varphi d\theta}{A^2} \qquad with \quad \{(\theta_0, \varphi_0), (\pi + \theta_0, \varphi_0)\}$$

we can have

$$V = \kappa \int_{-\frac{\pi}{2}}^{+\frac{\pi}{2}} \int_0^{2\pi} \left(\frac{\cos^2 \varphi \cos^2 \theta}{a^2} \cdot \frac{x^2}{a^2} + \frac{\cos^2 \varphi \sin^2 \theta}{b^2} \cdot \frac{y^2}{b^2} + \frac{\sin^2 \varphi}{c^2} \cdot \frac{z^2}{c^2} \right) \frac{\cos \varphi d\varphi d\theta}{A^2}$$
$$- \frac{\kappa}{2} C \int_{-\frac{\pi}{2}}^{+\frac{\pi}{2}} \int_0^{2\pi} \frac{\cos \varphi d\varphi d\theta}{A} \tag{.12}$$

To further simplify the above expression, one may use the following:

$$W = \frac{\kappa}{2} \int_{-\frac{\pi}{2}}^{+\frac{\pi}{2}} \int_0^{2\pi} \frac{\cos \varphi d\varphi d\theta}{A} \tag{.13}$$

The simplified form of the potential then reduces to:

$$V = \frac{1}{a} \frac{\partial W}{\partial a} x^2 + \frac{1}{b} \frac{\partial W}{\partial b} y^2 + \frac{1}{c} \frac{\partial W}{\partial c} z^2 - CW$$
$$= \left(\frac{1}{a} \frac{\partial W}{\partial a} - \frac{W}{a^2} \right) x^2 + \left(\frac{1}{b} \frac{\partial W}{\partial b} - \frac{W}{b^2} \right) y^2 + \left(\frac{1}{c} \frac{\partial W}{\partial c} - \frac{W}{c^2} \right) z^2 + W \tag{.14}$$

Since W is a function of the semi-axes (a, b, c), then so are all of its derivatives. Therefore, the coefficients of the quadratic term x^2, y^2 and z^2 are functions of a, b, and c only. Also, W is the potential at the center of the ellipsoid if taking $P(x, y, z) = (0, 0, 0)$.

We can simplify the expression of W with the help of the following substitution:

$$M = \frac{\cos^2 \varphi}{a^2} + \frac{\sin^2 \varphi}{c^2} \tag{.15a}$$

$$N = \frac{\cos^2 \varphi}{b^2} + \frac{\sin^2 \varphi}{c^2} \tag{.15b}$$

92

Eq..13 then becomes

$$
\begin{aligned}
W &= \frac{\kappa}{2} \int_{-\frac{\pi}{2}}^{+\frac{\pi}{2}} \cos\varphi d\varphi \int_0^{2\pi} \frac{d\theta}{M\cos^2\theta + N\sin^2\theta} \\
&= 4\kappa \int_0^{\frac{\pi}{2}} \cos\varphi d\varphi \int_0^{\frac{\pi}{2}} \frac{\sec^2\theta d\theta}{M + N\tan^2\theta} \\
&= 2\pi\kappa \int_0^{\frac{\pi}{2}} \frac{\cos\varphi d\varphi}{\sqrt{MN}} \\
&= 2\pi\kappa abc^2 \int_0^{\frac{\pi}{2}} \frac{\cos\varphi d\varphi}{\sqrt{(a^2\sin^2\varphi + c^2\cos^2\varphi)(b^2\sin^2\varphi + c^2\cos^2\varphi)}}
\end{aligned}
\tag{.16}
$$

To restore the symmetry within a, b, and c, we can introduce the following substitution:

$$
\sin\varphi = \frac{c}{\sqrt{c^2 + s}} \qquad \Rightarrow \qquad \frac{d\sin\varphi}{ds} = -\frac{c}{2(c^2 + s)^{3/2}}
\tag{.17}
$$

where s is the new variable of integration. Eventually, W can be written as:

$$
W = \pi\kappa abc \int_0^\infty \frac{ds}{\sqrt{(a^2 + s)(b^2 + s)(c^2 + s)}}
\tag{.18}
$$

with the term related to the derivative of W with respect to a reads:

$$
\begin{aligned}
\frac{1}{a}\frac{\partial W}{\partial a} - \frac{W}{a^2} &= \frac{\pi\kappa abc}{a^2} \int_0^\infty \left(\frac{\partial a(a^2 + s)^{-\frac{1}{2}}}{\partial a} - \frac{1}{\sqrt{a^2 + s}} \right) \frac{ds}{\sqrt{(b^2 + s)(c^2 + s)}} \\
&= -\pi\kappa abc \int_0^\infty \frac{1}{a^2 + s} \frac{ds}{\sqrt{(a^2 + s)(b^2 + s)(c^2 + s)}}
\end{aligned}
\tag{.19}
$$

Therefore, the potential inside of a uniform ellipsoidal electron bunch may be expressed as:

$$
V(x, y, z) = \frac{\rho_c}{4\varepsilon_0} abc \int_0^\infty \left(1 - \frac{x^2}{a^2 + s} - \frac{y^2}{b^2 + s} - \frac{z^2}{c^2 + s} \right) \frac{ds}{\sqrt{(a^2 + s)(b^2 + s)(c^2 + s)}}
\tag{.20}
$$

with zero point of potential at infinity.

The corresponding electrostatic field at the interior point $P(x, y, z)$ is,

$$\vec{E}(x, y, z) = E_x \hat{x} + E_y \hat{y} + E_z \hat{z} \tag{.21}$$

with $\hat{x}$, $\hat{y}$, and $\hat{z}$ representing the unit vectors, respectively. The components of the field can be represented by the following equations:

$$E_x(x, y, z) = x \cdot \frac{\rho_c abc}{2\varepsilon_0} \int_0^\infty \frac{ds}{(a^2 + s)\sqrt{(a^2 + s)(b^2 + s)(c^2 + s)}} \tag{.22a}$$

$$E_y(x, y, z) = y \cdot \frac{\rho_c abc}{2\varepsilon_0} \int_0^\infty \frac{ds}{(b^2 + s)\sqrt{(a^2 + s)(b^2 + s)(c^2 + s)}} \tag{.22b}$$

$$E_z(x, y, z) = z \cdot \frac{\rho_c abc}{2\varepsilon_0} \int_0^\infty \frac{ds}{(c^2 + s)\sqrt{(a^2 + s)(b^2 + s)(c^2 + s)}} \tag{.22c}$$

BIBLIOGRAPHY

BIBLIOGRAPHY

[1] J. M. E. Portman, *Ultrafast Science: A Multiscale Modeling Approach to Femtosecond Electron Diffraction and Its Applications.* PhD thesis, Michigan State University, 2014.

[2] W. E. King, G. H. Campbell, A. Frank, B. Reed, J. F. Schmerge, B. J. Siwick, B. C. Stuart, and P. M. Weber, "Ultrafast electron microscopy in materials science, biology, and chemistry," *J. Appl. Phys.*, vol. 97, p. 111101, June 2005.

[3] Z. Tao, *Development of High-Brightness Ultrafast Electron Microscope for Studying Nanoscale Dynamics Associated with Strongly Correlated Materials.* PhD thesis, Michigan State University, 2014.

[4] R. D. Miller, "Mapping Atomic Motions with Ultrabright Electrons: The Chemists' Gedanken Experiment Enters the Lab Frame," *Annu. Rev. Phys. Chem.*, vol. 65, pp. 583–604, Apr. 2014.

[5] R. J. D. Miller, "Femtosecond Crystallography with Ultrabright Electrons and X-rays: Capturing Chemistry in Action," *Science*, vol. 343, pp. 1108–1116, Mar. 2014.

[6] C.-Y. Ruan, F. Vigliotti, V. A. Lobastov, S. Chen, and A. H. Zewail, "Ultrafast electron crystallography: Transient structures of molecules, surfaces, and phase transitions," *Proceedings of the National Academy of Sciences*, vol. 101, pp. 1123–1128, Feb. 2004.

[7] P. Baum, D.-S. Yang, and A. H. Zewail, "4D Visualization of Transitional Structures in Phase Transformations by Electron Diffraction," *Science*, vol. 318, pp. 788–792, Nov. 2007.

[8] P. Baum and A. Zewail, "Femtosecond diffraction with chirped electron pulses," *Chem. Phys. Lett.*, vol. 462, pp. 14–17, Sept. 2008.

[9] M. Harb, R. Ernstorfer, C. T. Hebeisen, G. Sciaini, W. Peng, T. Dartigalongue, M. A. Eriksson, M. G. Lagally, S. G. Kruglik, and R. J. D. Miller, "Electronically Driven Structure Changes of Si Captured by Femtosecond Electron Diffraction," *Phys. Rev. Lett.*, vol. 100, p. 155504, Apr. 2008.

[10] A. H. Zewail, "Four-Dimensional Electron Microscopy," *Science*, vol. 328, pp. 187–193, Apr. 2010.

[11] A. Feist, *Next-Generation Ultrafast Transmission Electron Microscopy – Development and Applications.* PhD thesis, Georg-August-Universität Göttingen, Göttingen, Germany, 2018.

[12] R. K. Raman, R. A. Murdick, R. J. Worhatch, Y. Murooka, S. D. Mahanti, T.-R. T. Han, and C.-Y. Ruan, "Electronically Driven Fragmentation of Silver Nanocrystals Revealed by Ultrafast Electron Crystallography," *Phys. Rev. Lett.*, vol. 104, p. 123401, Mar. 2010.

[13] Z. Tao, H. Zhang, P. M. Duxbury, M. Berz, and C.-Y. Ruan, "Space charge effects in ultrafast electron diffraction and imaging," *Journal of Applied Physics*, vol. 111, p. 044316, Feb. 2012.

[14] J. Portman, H. Zhang, Z. Tao, K. Makino, M. Berz, P. M. Duxbury, and C.-Y. Ruan, "Computational and experimental characterization of high-brightness beams for femtosecond electron imaging and spectroscopy," *Appl. Phys. Lett.*, vol. 103, no. 25, p. 253115, 2013.

[15] C. Kiseok, *Development of a High-Brightness Electron Beam System towards Femtosecond Microdiffraction and Imaging and Its Applications.* PhD thesis, Michigan State University, 2014.

[16] J. Portman, H. Zhang, K. Makino, C. Y. Ruan, M. Berz, and P. M. Duxbury, "Untangling the contributions of image charge and laser profile for optimal photoemission of high-brightness electron beams," *J. Appl. Phys.*, vol. 116, p. 174302, Nov. 2014.

[17] B. S. Zerbe, X. Xiang, C.-Y. Ruan, S. M. Lund, and P. M. Duxbury, "Dynamical bunching and density peaks in expanding Coulomb clouds," *Phys. Rev. Accel. Beams*, vol. 21, p. 064201, June 2018.

[18] J. Williams, F. Zhou, T. Sun, Z. Tao, K. Chang, K. Makino, M. Berz, P. M. Duxbury, and C.-Y. Ruan, "Active control of bright electron beams with RF optics for femtosecond microscopy," *Struct. Dyn.*, vol. 4, p. 044035, July 2017.

[19] A. A. Ischenko, I. V. Kochikov, and R. J. D. Miller, "The effect of Coulomb repulsion on the space-time resolution limits for ultrafast electron diffraction," *J. Chem. Phys.*, vol. 150, p. 054201, Feb. 2019.

[20] F. Zhou, *Non-Equilibrium Phase Transformations in Charge-Density Wave and Strongly Correlated Systems Studied by Coherent Femtosecond Electron Diffraction.* PhD thesis, Michigan State University, 2019.

[21] O. J. Luiten, S. B. van der Geer, M. J. de Loos, F. B. Kiewiet, and M. J. van der Wiel, "How to Realize Uniform Three-Dimensional Ellipsoidal Electron Bunches," *Phys. Rev. Lett.*, vol. 93, Aug. 2004.

[22] M. Grech, R. Nuter, A. Mikaberidze, P. Di Cintio, L. Gremillet, E. Lefebvre, U. Saalmann, J. M. Rost, and S. Skupin, "Coulomb explosion of uniformly charged spheroids," *Phys. Rev. E*, vol. 84, Nov. 2011.

[23] J. Rosenzweig, A. Cook, R. England, M. Dunning, S. Anderson, and M. Ferrario, "Emittance compensation with dynamically optimized photoelectron beam profiles," *Nucl. Instrum. Methods Phys. Res. Sect. Accel. Spectrometers Detect. Assoc. Equip.*, vol. 557, pp. 87–93, Feb. 2006.

[24] B. J. Claessens, S. B. van der Geer, G. Taban, E. J. D. Vredenbregt, and O. J. Luiten, "Ultracold Electron Source," *Phys. Rev. Lett.*, vol. 95, p. 164801, Oct. 2005.

[25] Y. Otake and B. J. Siwick, "Advanced diagnosis of the temporal characteristics of ultrashort electron beams," *Nucl. Instrum. Methods Phys. Res. Sect. Accel. Spectrometers Detect. Assoc. Equip.*, vol. 637, no. 1, pp. S7–S11, 2011.

[26] S. B. van der Geer, M. J. de Loos, T. van Oudheusden, W. P. E. M. op 't Root, M. J. van der Wiel, and O. J. Luiten, "Longitudinal phase-space manipulation of ellipsoidal electron bunches in realistic fields," *Phys. Rev. Spec. Top. - Accel. Beams*, vol. 9, p. 044203, Apr. 2006.

[27] P. Musumeci, J. T. Moody, R. J. England, J. B. Rosenzweig, and T. Tran, "Experimental Generation and Characterization of Uniformly Filled Ellipsoidal Electron-Beam Distributions," *Phys. Rev. Lett.*, vol. 100, p. 244801, June 2008.

[28] C. C. Lin, L. Mestel, and F. H. Shu, "The Gravitational Collapse of a Uniform Spheroid.," *The Astrophysical Journal*, vol. 142, p. 1431, Nov. 1965.

[29] P. Di Cintio, *Dynamics of Heterogeneous Clusters under Intense Laser Fields.* PhD thesis, Technische Universität Dresden, Dresden, Germany, 2014.

[30] A. M. Michalik and J. E. Sipe, "Analytic model of electron pulse propagation in ultrafast electron diffraction experiments," *J. Appl. Phys.*, vol. 99, no. 5, p. 054908, 2006.

[31] A. M. Michalik, E. Y. Sherman, and J. E. Sipe, "Theory of ultrafast electron diffraction: The role of the electron bunch properties," *J. Appl. Phys.*, vol. 104, no. 5, p. 054905, 2008.

[32] J. A. Berger and W. A. Schroeder, "Semianalytic model of electron pulse propagation: Magnetic lenses and rf pulse compression cavities," *J. Appl. Phys.*, vol. 108, p. 124905, Dec. 2010.

[33] Kapchinskij and Vladimirskij, "Limitations of Proton Beam Current in a Strong Focusing Linear Accelerator Associated With the Beam Space Charge," in *Proceedings*, (Geneva, Switzerland), pp. 274–287, CERN, 1959.

[34] F. J. Sacherer, "RMS Envelope Equations with Space Charge," *IEEE Trans. Nucl. Sci.*, vol. 18, no. 3, pp. 1105–1107, 1971.

[35] X. Xiang, B. Zerbe, and P. M. Duxbury, "Crossover and the dynamics of uniform electron ellipsoids focused by linear chirp," working paper, Michigan State University, 2020.

[36] W. MacMillan, *The Theory of the Potential.* MacMillan's Theoretical Mechanics, New York, NY: Dover, 1958.

[37] R. Gluckstren, "Scalar Potential for Charge Distributions With Ellipsoidal Symmetry," tech. rep., Physics Department, University of Maryland, Fermilab, May 1986.

[38] O. D. Kellogg, *Foundations of Potential Theory.* Berlin, Heidelberg: Springer Berlin Heidelberg, 1967.

[39] Landau and Lifshitz, *Electrodynamics Of Continuous Media*, vol. 8 of *Course of Theoretical Physics.* Pergamon Press, 1960.

[40] J. Buon, "Beam Phase Space and emittance," tech. rep., Paris-11 Univ., 1992.

[41] B. S. Zerbe, X. Xiang, J. Williams, C.-Y. Ruan, and P. M. Duxbury, "Mean-field space charge effects on longitudinally focussed electron bunches," working paper, Michigan State University, Nov. 2019.

[42] Z. Gimbutas and L. Greengard, "Computational Software: Simple FMM Libraries for Electrostatics, Slow Viscous Flow, and Frequency-Domain Wave Propagation," *Commun. Comput. Phys.*, vol. 18, pp. 516–528, Aug. 2015.

[43] R. Beatson and L. Greengard, "A short course on fast multipole methods," *Wavelets Multilevel Methods Elliptic PDEs*, vol. 1, pp. 1–37, 1997.

[44] B. A. Luty, M. E. Davis, I. G. Tironi, and W. F. Van Gunsteren, "A Comparison of Particle-Particle, Particle-Mesh and Ewald Methods for Calculating Electrostatic Interactions in Periodic Molecular Systems," *Molecular Simulation*, vol. 14, pp. 11–20, Dec. 1994.

[45] S. Plimpton, "Fast Parallel Algorithms for Short–Range Molecular Dynamics," *J. Comput. Phys.*, vol. 117, p. 42, Mar. 1995.

[46] M. Reiser, *Theory and Design of Charged Particle Beams.* Weinheim: Wiley-VCH, second ed., 2008.

[47] D. Gericke and M. Murillo, "Disorder-induced heating of ultracold plasmas," *Contrib. Plasma Phys.*, vol. 43, pp. 298–301, Oct. 2003.

[48] M. S. Murillo, "Ultrafast Dynamics of Strongly Coupled Plasmas," *Phys. Rev. Lett.*, vol. 96, p. 165001, Apr. 2006.

[49] M. S. Murillo, "Ultrafast dynamics of neutral, ultracold plasmas," *Physics of Plasmas*, vol. 14, p. 055702, May 2007.

[50] M. Lyon and S. D. Bergeson, "The influence of electron screening on disorder-induced heating," *J. Phys. B: At. Mol. Opt. Phys.*, vol. 44, p. 184014, Sept. 2011.

[51] D. Murphy, R. E. Scholten, and B. M. Sparkes, "Increasing the Brightness of Cold Ion Beams by Suppressing Disorder-Induced Heating with Rydberg Blockade," *Phys. Rev. Lett.*, vol. 115, p. 214802, Nov. 2015.

[52] B. J. Siwick, J. R. Dwyer, R. E. Jordan, and R. J. D. Miller, "Ultrafast electron optics: Propagation dynamics of femtosecond electron packets," *J. Appl. Phys.*, vol. 92, no. 3, p. 1643, 2002.

[53] M. Kuwahara, Y. Nambo, K. Aoki, K. Sameshima, X. Jin, T. Ujihara, H. Asano, K. Saitoh, Y. Takeda, and N. Tanaka, "The Boersch effect in a picosecond pulsed electron beam emitted from a semiconductor photocathode," *Appl. Phys. Lett.*, vol. 109, p. 013108, July 2016.

[54] Y. Zou, Y. Cui, M. Reiser, and P. G. O'Shea, "Observation of the Anomalous Increase of the Longitudinal Energy Spread in a Space-Charge-Dominated Electron Beam," *Phys. Rev. Lett.*, vol. 94, Apr. 2005.

[55] G. H. Jansen, *Coulomb Interactions in Particle Beams*. Advances in Electronics & Electron Physics, Academic Pr, 1990.

[56] S. D. Berger, "Particle–particle interaction effects in image projection lithography systems," *J. Vac. Sci. Technol. B Microelectron. Nanometer Struct.*, vol. 11, p. 2294, Nov. 1993.

[57] P. Hawkes and E. Kasper, "Space Charge Effects," in *Principles of Electron Optics*, pp. 1101–1130, Elsevier, 2018.

[58] M. M. Mkrtchyan, J. A. Liddle, S. D. Berger, L. R. Harriott, J. M. Gibson, and A. M. Schwartz, "Stochastic scattering in charged particle projection systems: A nearest neighbor approach," *J. Appl. Phys.*, vol. 78, pp. 6888–6902, Dec. 1995.

[59] A. W. Hyatt, C. F. Driscoll, and J. H. Malmberg, "Measurement of the Anisotropic Temperature Relaxation Rate in a Pure Electron Plasma," *Phys. Rev. Lett.*, vol. 59, pp. 2975–2978, Dec. 1987.

[60] S. Ichimaru, "Relaxation Processes in Plasmas with Magnetic Field. Temperature Relaxations," *Phys. Fluids*, vol. 13, no. 11, p. 2778, 1970.